Flexible Aircraft Gust Load Alleviation with Incremental Nonlinear Dynamic Inversion

Wang, Xuerui; van Kampen, Erik-Jan; Chu, Qiping; De Breuker, Roeland

DOI
10.2514/6.2018-0774

Publication date
2018

Document Version
Final published version

Published in
Proceedings of the 2018 AIAA Atmospheric Flight Mechanics Conference

AIAA SciTech Forum
8–12 January 2018, Kissimmee, Florida
2018 AIAA Atmospheric Flight Mechanics Conference

10.2514/6.2018-0774

Flexible Aircraft Gust Load Alleviation with Incremental Nonlinear Dynamic Inversion

Xuerui Wang*, Erik-Jan van Kampen†, Qiping Chu‡, Roeland De Breuker§
Delft University of Technology, Delft, Zuid-Holland, 2629HS, The Netherlands

In this paper, an Incremental Nonlinear Dynamic Inversion (INDI) controller is developed for the flexible aircraft gust load alleviation (GLA) problem. First, a flexible aircraft model captures both inertia and aerodynamic coupling effects between flight dynamics and structural vibration dynamics is presented. Then an INDI GLA controller is designed for this aircraft model based on sensor measurements and the Kalman filter online estimation. Besides, the fifth order Padé approximation is used to model the pure time delay in the state estimation. Furthermore, simulations of the flexible aircraft flying through various spatial turbulence and gust fields demonstrate the effectiveness of the proposed controller on rigid-body motion regulation, vertical load alleviation, wing root bending moment reduction and elastic modes suppression. Additionally, numerical perturbation tests and a Monte-Carlo study show the robustness of the proposed controller to aerodynamic model uncertainties.

*PhD Candidate, Control and Simulation Section, Faculty of Aerospace Engineering, Delft University of Technology; Kluyverweg 1, 2629HS, Delft, The Netherlands. X.Wang-6@tudelft.nl.

†Assistant Professor, Control and Simulation Section, Faculty of Aerospace Engineering, Delft University of Technology; Kluyverweg 1, 2629HS, Delft, The Netherlands, E.vanKampen@tudelft.nl, Member AIAA.

‡Associate Professor, Control and Simulation Section, Faculty of Aerospace Engineering, Delft University of Technology; Kluyverweg 1, 2629HS, Delft, The Netherlands, Q.P.Chu@tudelft.nl, Member AIAA.

§Associate Professor, Aerospace Structures and Computational Mechanics, Faculty of Aerospace Engineering, Delft University of Technology; Kluyverweg 1, 2629HS, Delft, The Netherlands, R.DeBreuker@tudelft.nl.

Nomenclature

C_w	=	matrix of direction cosines between (x_w, y_w, z_w) and (x_f, y_f, z_f)
C_f	=	matrix of direction cosines between (x_f, y_f, z_f) and (X_E, Y_E, Z_E)
C_e	=	matrix of direction cosines between (x_e, y_e, z_e) and (x_f, y_f, z_f)
C_{uw}, $C_{\psi w}$	=	damping matrices for the bending and torsion of the wing
EI, GJ	=	bending and torsion stiffness, N·m^2
E_f	=	matrix relating Eulerian velocities to angular quasi-velocities
$\mathbf{f}_f$, $\mathbf{f}_w$, $\mathbf{f}_e$	=	distributed forces on fuselage, wing and empennage
$\mathbf{F}$, $\mathbf{M}$	=	generalized resultant forces and moments, N, N·m
$\mathcal{F}_{uw}$, $\mathcal{F}_{\alpha w}$	=	Ratleigh's dissipation function densities
G	=	control effectiveness matrix
J	=	inertia matrix for the deformed aircraft
$\mathcal{K}_{uw}$, $\mathcal{K}_{\psi w}$	=	stiffness matrices for the bending and torsion of the wing
L	=	Lagrangian for the aircraft
$\mathcal{L}$, $\mathcal{H}$	=	matrices of stiffness differential operators for the wing
M	=	system mass matrix
M_r	=	wing root bending moment, N·m
n_z	=	vertical load, g
$\mathbf{p}_{V_f}$, $\mathbf{p}_{\omega_f}$, $\mathbf{p}_{uw}$, $\mathbf{p}_{\psi w}$	=	momentum vectors for aircraft translation, rotation, bending, and torsion
$\boldsymbol{q}$, $\boldsymbol{\xi}$	=	vectors of generalized coordinates for the bending and torsion
$\mathbf{r}_w$, $\mathbf{r}_f$, $\mathbf{r}_e$	=	nominal position vector of a point on the wing, fuselage, and tail, m
$\mathbf{r}_{fw}$	=	radius vector from O_f to O_w, m
$\mathbf{r}_{fe}$	=	radius vector from O_f to O_e, m
$\boldsymbol{R}_f$	=	position vector of the origin of (x_f, y_f, z_f) relative to (X_E, Y_E, Z_E), m
$\boldsymbol{s}$, $\boldsymbol{\eta}$	=	vectors of generalized coordinates for the bending and torsion velocities
$\tilde{S}$	=	matrix of the first moments of inertia of the deformed aircraft
$\mathcal{T}$, $\mathcal{V}$	=	kinetic, potential energy of the aircraft
$\mathbf{u}_w$, $\boldsymbol{\psi}_w$	=	bending and torsion displacements of the wing, m, rad
$\hat{\mathbf{U}}$, $\hat{\boldsymbol{\Psi}}$	=	resultant of force and moment density vectors
$\mathbf{v}_w$, $\boldsymbol{\alpha}_w$	=	bending and torsion velocities of the wing, m/s, rad/s
$\boldsymbol{V}_f$	=	translational velocity vectors of (x_f, y_f, z_f), m/s
$\boldsymbol{x}_{rm}$	=	state reference vector
$\boldsymbol{x}_r$, $\boldsymbol{x}_e$	=	rigid and elastic states vector
$\boldsymbol{\theta}_f$	=	Euler angles vector, rad
$\boldsymbol{\omega}_f$	=	angular velocity vector of (x_f, y_f, z_f), rad/s
$\bar{\mathbf{v}}_w$, $\bar{\mathbf{v}}_f$, $\bar{\mathbf{v}}_e$	=	velocity of an arbitrary mass element on the wing, fuselage, and tail, m/s
Φ, Ψ	=	shape function matrices of the bending and torsion
$\boldsymbol{\delta}$	=	control vector
$\boldsymbol{\nu}$	=	virtual control vector
$\Delta\boldsymbol{u}$	=	incremental control input
$\Delta\boldsymbol{x}$	=	incremental state variation vector

I. Introduction

While enjoying the aerodynamic benefits provided by light-weight composite materials, aircraft designers are facing the challenges of the accompanying greater structural flexibility. As the structural flexibility increases, not only the interactions between aerodynamics and structural vibration dynamics become significant, which are within the category of aeroelasticity discipline, the coupling effects between rigid-body dynamics and structural vibration dynamics are also non-negligible.

In order to capture these interactions, a multidisciplinary modeling framework integrating nonlinear flight dynamics, aerodynamics and structural vibration dynamics is required. The mean axes method was introduced by Schmidt et al. [1] to avoid the inertia couplings between rigid-body motions and structural vibrations, resulting in classical flight dynamic equations augmented with a series of second-order linear

differential equations representing the structural dynamics. However, the constrains defining these axes are tedious to enforce [2]. A more rigorous approach using body-fixed axes and based on Lagrange's equations in quasi-coordinates was developed by Meirovitch et al. [2]. This approach results in a fully nonlinear system including both inertial and aerodynamic coupling effects. The inertial coupling effects can be significant for very flexible aircraft. With the wing stiffness further been reduced, the geometrically nonlinear aeroelasticity needs to be modeled, which shows significant influences on flight dynamic modes [3]. Strain-based approaches are widely used for highly flexible aircraft modeling [3, 4]. Although the linearized analyses around the nonlinear equilibrium points are providing sound aircraft designs, nonlinear control methods are promising for controlling the nonlinear dynamics contributed by both flight dynamics and nonlinear aeroelasticity.

The reduced structural rigidity also influences the stability and dynamic responses of the aircraft. When a flexible aircraft encounters atmospheric disturbances, both the rigid-body and structural modes are excited, which degrade ride quality, deviate flight trajectory, introduce extra structural loads, shorten structural fatigue life, and even threaten flight safety. Integrated active flight control that deals with both rigid-body and structural dynamics is a promising way to alleviate gust loads and improve ride quality. The Linear Quadratic Gaussian (LQG) method is broadly used for the gust load alleviation (GLA) and flutter suppression of the flexible aircraft [5–7]. Haghighat et al. [8] designed a model-predictive controller with an additional feedback loop to increase the prediction accuracy, which is proven to perform better than a Linear Quadratic Regular (LQR) controller. A mixed norm H_2/H_∞ fault tolerant controller is designed to alleviate the gust loads of a flexible aircraft subject to loss of control effectiveness [9]. Adaptive feedforward control method can make full use of the gust velocity measurements (by using the LIDAR beam airbone wind sensor [10], pitot tube, etc.) and is adopted by Zeng et al. [10] for GLA problems.

Different from model-based control methods, the Incremental Nonlinear Dynamic Inversion (INDI) is a sensor-based approach, which improves the robust performance of the system without using any robust, adaptive or intelligent control algorithms [11–15]. The INDI GLA control law has been developed for a quasi-rigid aircraft [13] and shows better GLA performance, task applicability, robustness and command tracking under disturbances as compared to a LQR controller. This paper extends the previous work [13] to the flexible aircraft GLA problem. New research questions arise when solving the flexible aircraft GLA problem using the INDI method. The first doubt is the applicability of the time scale separation principle [11–15] for flexible aircraft, since the elastic modes have higher frequencies as compared to rigid-body modes. As a result, the elastic modes may not be omitted in the incremental dynamic equations. Besides, the equations of motion integrating flight dynamics and structural dynamics are of high order, so traditional aircraft control surfaces (elevator, rudder and ailerons) would be inadequate to achieve a decoupled control of different control goals, so trade-offs should be made for the flexible aircraft INDI GLA controller. Finally, the INDI GLA control law requires the feedback of states and state derivatives. Although the measurements and estimations of rigid-body states and state derivatives have been discussed previously [11–15], a method that can estimate the elastic states and their derivatives need to be developed. These research questions will be answered in this paper.

The main contributions of this paper are: (1) An INDI GLA control framework designed for flexible aircraft aiming at rigid-body modes regulation, vertical load alleviation, wing root bending moment reduction and elastic modes suppression. The time scale separation principle is redefined for flexible aircraft and verified numerically. Also, the virtual control for this underdetermined system is allocated to the control surfaces using weighted least squares method. (2) A Kalman filter optimal observer designed to estimate the elastic states online. The fifth order Padé approximation is used to model the pure time delay in the estimation. (3) Numerical perturbation tests and a Monte-Carlo study to demonstrate the robust performance of the proposed controller.

This paper is organized as follows: Sec. II sets up the Equations of Motion (EQM) of the flexible aircraft as well as the gust and turbulence models. Sec. III derives the INDI GLA control law with the simulation results shown and discussed in Sec. IV. Main conclusions are drawn in Sec. V.

$$
\begin{aligned}
\frac{d}{dt}\left(\frac{\partial L}{\partial \boldsymbol{V}_f}\right) + \tilde{\omega}_f \frac{\partial L}{\partial \boldsymbol{V}_f} - C_f \frac{\partial L}{\partial \boldsymbol{R}_f} &= \mathbf{F} \\
\frac{d}{dt}\left(\frac{\partial L}{\partial \boldsymbol{\omega}_f}\right) + \tilde{V}_f \frac{\partial L}{\partial \boldsymbol{V}_f} + \tilde{\omega}_f \frac{\partial L}{\partial \boldsymbol{\omega}_f} - E_f^{-T} \frac{\partial L}{\partial \boldsymbol{\theta}_f} &= \mathbf{M} \\
\frac{\partial}{\partial t}\left(\frac{\partial \hat{L}}{\partial \mathbf{v}_w}\right) - \frac{\partial \hat{L}}{\partial \mathbf{u}_w} + \frac{\partial \hat{\mathcal{F}}_{uw}}{\partial \dot{\mathbf{u}}_w} + \mathcal{L}\mathbf{u}_w &= \hat{\mathbf{U}} \\
\frac{\partial}{\partial t}\left(\frac{\partial \hat{L}}{\partial \boldsymbol{\alpha}_w}\right) + \frac{\partial \hat{\mathcal{F}}_{\alpha_w}}{\partial \dot{\boldsymbol{\psi}}_w} + \mathcal{H}\boldsymbol{\psi}_w &= \hat{\boldsymbol{\Psi}} \qquad (1)
\end{aligned}
$$

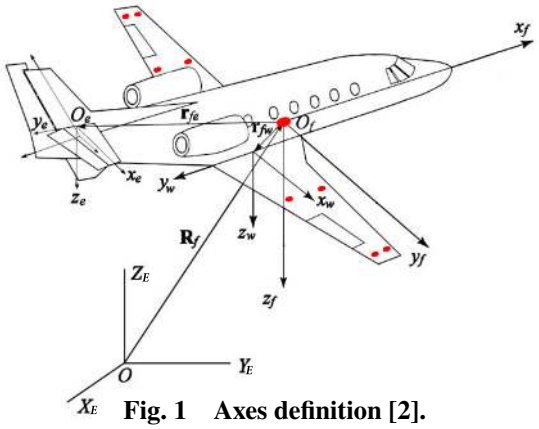

Fig. 1 Axes definition [2].

II. Flexible Aircraft and Gust Models

A. Flexible Aircraft EQM

The flexible aircraft modeled here is a simplified form of the model given in [2], only the right and left wings are assumed to be flexible, undergoing bending and torsion deformations, modeled as cantilever beams. The remaining components, namely fuselage and empennage (horizontal and vertical tails) are assumed to be rigid. A set of body-fixed axes (x_i, y_i, z_i), $i = f, w, e$ are attached to the undeformed aircraft as shown by Fig. 1. Generic Lagrangian equations of motion in quasi-coordinates are given in Eq. (1) [2].

In Eq. (1), $L = \mathcal{T} - \mathcal{V}$ represents the Lagrangian energy for the whole aircraft. $\boldsymbol{V}_f$ and $\boldsymbol{\omega}_f$ represent the (x_f, y_f, z_f) axes translational and rotational velocities, while $\boldsymbol{R}_f$ and $\boldsymbol{\theta}_f$ indicate the position and Euler angles of the (x_f, y_f, z_f) axes relative to (X_E, Y_E, Z_E). $\mathbf{F}$ and $\mathbf{M}$ are the total forces and moments, while $\hat{\mathbf{U}}$ and $\hat{\boldsymbol{\Psi}}$ are the resultant of force and moment density vectors. $C_f(\phi, \theta, \psi)$ is the rotation transformation matrix from inertial axes (X_E, Y_E, Z_E) to (x_f, y_f, z_f), and the $E(\phi, \theta)$ matrix links angular velocities $\boldsymbol{\omega}_f$ to Eulerian velocities $\dot{\boldsymbol{\theta}}_f$. Bold mark indicates a vector. $\hat{(\cdot)}$ indicates the volume density of energy terms and $\tilde{(\cdot)}$ refers to the skew-symmetric matrix of a vector. $\mathcal{L}$ and $\mathcal{H}$ are matrices of stiffness differential operators, with $\mathcal{F}_{uw}$ and $\mathcal{F}_{\alpha w}$ represent the Ratleigh's dissipation function densities. $\mathbf{u}_w$ and $\mathbf{v}_w = \dot{\mathbf{u}}_w$ represent elastic bending displacement and velocity vectors, while $\boldsymbol{\psi}_w$ and $\boldsymbol{\alpha}_w = \dot{\boldsymbol{\psi}}_w$ represent elastic torsion angle and angular velocity vectors. Galerkin method is used to discretize the flexible displacements in modal form as

$$
\begin{aligned}
\mathbf{u}_w(\mathbf{r}_w, t) &= \Phi(\mathbf{r}_w)\boldsymbol{q}(t), \quad \dot{\boldsymbol{q}}(t) = \boldsymbol{s}(t) \\
\boldsymbol{\psi}_w(\mathbf{r}_w, t) &= \Psi(\mathbf{r}_w)\boldsymbol{\xi}(t), \quad \dot{\boldsymbol{\xi}}(t) = \boldsymbol{\eta}(t)
\end{aligned} \qquad (2)
$$

where $\Phi(\mathbf{r}_w)$ and $\Psi(\mathbf{r}_w)$ are bending and torsion shape function matrices respectively. $\mathbf{r}_{fw}$ and $\mathbf{r}_{fe}$ represent relative distances of component axes. C_w and C_e refer to the coordinates transformation matrices. The velocities of an infinitesimal mass element dm on the wing $\bar{\mathbf{v}}_w$, the fuselage $\bar{\mathbf{v}}_f$ and the tail $\bar{\mathbf{v}}_e$ can be expressed as

$$
\begin{aligned}
\bar{\mathbf{v}}_w(\mathbf{r}_w, t) &= C_w \boldsymbol{V}_f + C_w \tilde{r}_{fw}^T \boldsymbol{\omega}_f + (\tilde{r}_w + \widetilde{\Phi \boldsymbol{q}})^T C_w \boldsymbol{\omega}_f + \tilde{r}_w^T \Psi \boldsymbol{\eta} + \Phi \boldsymbol{s} \\
\bar{\mathbf{v}}_f(\mathbf{r}_f, t) &= \boldsymbol{V}_f + \tilde{r}_f^T \boldsymbol{\omega}_f \\
\bar{\mathbf{v}}_e(\mathbf{r}_e, t) &= \boldsymbol{V}_f + (\tilde{r}_{fe} + \widetilde{C_e^T r_e})^T \boldsymbol{\omega}_f
\end{aligned} \qquad (3)
$$

Using Eq. (3), the total kinetic energy of the aircraft is

$$
\mathcal{T} = \sum_i \mathcal{T}_i = \frac{1}{2}\mathbf{V}^T M \mathbf{V}, \quad \mathcal{T}_i = \frac{1}{2}\int \bar{\mathbf{v}}_i^T \bar{\mathbf{v}}_i \, dm_i, \quad i = f, w, e \qquad (4)
$$

in which $\mathbf{V} = [V_f^T\ \boldsymbol{\omega}_f^T\ \boldsymbol{s}^T\ \boldsymbol{\eta}^T]^T$, M is the system mass matrix varies with deformations given as

$$M = \left[\begin{array}{cc:cc} mI_{3\times3} & \tilde{S}^T & C_w^T\int\Phi dm_w & C_w^T\int\tilde{r}_w^T\Psi dm_w \\ & J & C_w^T\int(\tilde{r}_w+\widetilde{\Phi\boldsymbol{q}})\Phi dm_w & C_w^T\int(\tilde{r}_w+\widetilde{\Phi\boldsymbol{q}})\tilde{r}_w^T\Psi dm_w \\ \hdashline & & \int\Phi^T\Phi dm_w & \int\Phi^T\tilde{r}_w^T\Psi dm_w \\ symmetric & & & \int\Psi^T\tilde{r}_w\tilde{r}_w^T\Psi dm_w \end{array}\right] = \left[\begin{array}{c:c} M_{rr} & M_{re} \\ \hdashline M_{er} & M_{ee} \end{array}\right] \tag{5}$$

with $\tilde{S}$ represents the matrix of first moment of area, and J represents moment of inertia of the deformed aircraft defined as

$$\begin{aligned} \tilde{S} &= \int\tilde{r}_f dm_f + \int\tilde{r}_{fe}dm_e + \int C_e^T\tilde{r}_e C_e dm_e + \int\tilde{r}_{fw}dm_w + \int C_w^T(\tilde{r}_w+\widetilde{\Phi\boldsymbol{q}})^T C_w dm_w \\ J &= \int\tilde{r}_f^T\tilde{r}_f dm_f + \int[C_w\tilde{r}_{fw}^T + (\tilde{r}_w+\widetilde{\Phi\boldsymbol{q}})^T C_w]^T[C_w\tilde{r}_{fw}^T + (\tilde{r}_w+\widetilde{\Phi\boldsymbol{q}})^T C_w]dm_w \\ &+ \int[C_e\widetilde{r}_{fe}^T + \tilde{r}_e^T C_e]^T[C_e\widetilde{r}_{fe}^T + \tilde{r}_e^T C_e]dm_e \end{aligned} \tag{6}$$

The linear momentum of the aircraft $\mathbf{p} = [\mathbf{p}_{V_f}^T\ \mathbf{p}_{\omega_f}^T\ \mathbf{p}_{uw}^T\ \mathbf{p}_{\psi w}^T]^T$ can be calculated as

$$\mathbf{p} = \frac{\partial\mathcal{T}}{\partial\mathbf{V}} = M\mathbf{V} \tag{7}$$

For the model in present paper, potential energy is purely due to wing deformation strain energy, which can be expressed as

$$\mathcal{V} = \frac{1}{2}(\boldsymbol{q}^T\mathcal{K}_{uw}\boldsymbol{q} + \boldsymbol{\xi}^T\mathcal{K}_{\psi w}\boldsymbol{\xi}),\ \ \mathcal{K}_{uw} = \int EI(\Phi'')^T\Phi''dx,\ \ \mathcal{K}_{\psi w} = \int GJ(\Psi')^T\Psi'dx \tag{8}$$

with EI and GJ refer to the bending and torsion stiffness. Assume structural damping matrices $C_{uw}, C_{\psi w}$ are proportional to $\mathcal{K}_{uw}, \mathcal{K}_{\psi w}$ respectively. Substituting Eqs. (2, 4, 7, 8) into Eq. (1), the system dynamics can be expressed in discrete form as [2]

$$\begin{aligned} \dot{\boldsymbol{R}}_f &= C_f^T\boldsymbol{V}_f \\ \dot{\boldsymbol{\theta}}_f &= E_f^{-1}\boldsymbol{\omega}_f \\ \dot{\mathbf{p}}_{V_f} &= -\tilde{\omega}_f\mathbf{p}_{V_f} + \mathbf{F}(\boldsymbol{V}_f, \boldsymbol{\omega}_f, \boldsymbol{q}, \boldsymbol{\xi}, \boldsymbol{s}, \boldsymbol{\eta}, \boldsymbol{\delta}, \boldsymbol{w}_g) \\ \dot{\mathbf{p}}_{\omega_f} &= -\tilde{V}_f\mathbf{p}_{V_f} - \tilde{\omega}_f\mathbf{p}_{\omega_f} + \mathbf{M}(\boldsymbol{V}_f, \boldsymbol{\omega}_f, \boldsymbol{q}, \boldsymbol{\xi}, \boldsymbol{s}, \boldsymbol{\eta}, \boldsymbol{\delta}, \boldsymbol{w}_g) \\ \dot{\mathbf{p}}_{uw} &= \frac{\partial\mathcal{T}}{\partial\boldsymbol{q}} - \mathcal{K}_{uw}\boldsymbol{q} - C_{uw}\boldsymbol{s} + \boldsymbol{Q}(\boldsymbol{V}_f, \boldsymbol{\omega}_f, \boldsymbol{q}, \boldsymbol{\xi}, \boldsymbol{s}, \boldsymbol{\eta}, \boldsymbol{\delta}, \boldsymbol{w}_g) \\ \dot{\mathbf{p}}_{\psi w} &= -\mathcal{K}_{\psi w}\boldsymbol{\xi} - C_{\psi w}\boldsymbol{\eta} + \boldsymbol{\Theta}(\boldsymbol{V}_f, \boldsymbol{\omega}_f, \boldsymbol{q}, \boldsymbol{\xi}, \boldsymbol{s}, \boldsymbol{\eta}, \boldsymbol{\delta}, \boldsymbol{w}_g) \end{aligned} \tag{9}$$

where $\frac{\partial\mathcal{T}}{\partial\boldsymbol{q}} = \frac{\partial\bar{\mathbf{v}}_w^T}{\partial\boldsymbol{q}}\frac{\partial\mathcal{T}}{\partial\bar{\mathbf{v}}_w} = \widetilde{\Phi C_w\omega_f}^T\int\bar{\mathbf{v}}_w dm_w$ includes Coriolis and centrifugal forces of the wing. $\boldsymbol{\delta} = [\delta_{a_s}, \delta_{a_a}, \delta_e, \delta_r, \delta_p]^T$ is the control vector, with $\delta_{a_s}, \delta_{a_a}$ represent the symmetric and asymmetric aileron deflection commands, and $\delta_e, \delta_r, \delta_p$ denote the elevator, rudder, and throttle control command respectively. $\boldsymbol{w}_g$ indicates the spacial turbulence field, which is a function of the aircraft position. The first two equations are referred to as the kinematic equations. The rest of equations are translational, rotational, bending and torsion dynamic equations respectively.

The generalized forces on the right-hand side can be obtained by means of virtual work, which are listed here for completeness [2].

$$\begin{aligned} \mathbf{F} &= \int_{D_f}[\mathbf{f}_f + \mathbf{F}_E\delta(\mathbf{r}-\mathbf{r}_E)]dD_f + C_w^T\int_{D_w}\mathbf{f}_w dD_w + C_e^T\int_{D_e}\mathbf{f}_e dD_e \\ \mathbf{M} &= \int_{D_f}\tilde{r}_f[\mathbf{f}_f + \mathbf{F}_E\delta(\mathbf{r}-\mathbf{r}_E)]dD_f + \int_{D_w}[\tilde{r}_{fw}C_w^T + C_w^T(\tilde{r}_w+\widetilde{\Phi\boldsymbol{q}})]\mathbf{f}_w dD_w + \int_{D_e}[\tilde{r}_{fe}C_e^T + C_e^T\tilde{r}_e]\mathbf{f}_e dD_e \\ \boldsymbol{Q} &= \int_{D_w}\Phi^T\mathbf{f}_w dD_w, \quad \boldsymbol{\Theta} = \int_{D_w}\Psi^T\tilde{r}_w\mathbf{f}_w dD_w \end{aligned} \tag{10}$$

$\mathbf{f}_f, \mathbf{f}_w, \mathbf{f}_e$ in Eq. (10) are distributed forces acting on fuselage, wing and empennage, which contain the aerodynamic, gravitational and control forces. The aerodynamic forces are calculated based on quasi-steady strip theory, and the local airspeed on each strip is perturbed by motions and gusts. δ represents the Dirac delta function. $\mathbf{F}_E$ indicates the thrust and $\mathbf{r}_E$ represents the engine position.

The main feature of the modeling approach in [2] is that the flight dynamics and structural vibration dynamics are coupled both inertially and aerodynamically. The aerodynamic couplings can be seen from the right-hand side of Eq. (9) where the generalized forces $\mathbf{F}, \mathbf{M}, \boldsymbol{Q}, \boldsymbol{\Theta}$ are functions of both the rigid-body and elastic states. The inertial couplings reflect on Eq. (5), where the off-diagonal blocks of the mass matrix M_{er}, M_{re} are non-zero. Also, in the rigid-body mass matrix M_{rr}, $\tilde{S}$ and J are functions of deformations as shown in Eq. (6). These inertial coupling effects can be considerable for highly flexible aircraft.

B. Gust and Turbulence Model

Two methods are often used to model the atmospheric disturbances, namely stochastic continuous turbulence and the deterministic discrete gust. The continuous turbulence is often simplified into stationary, homogeneous, isotropic stochastic process with Gaussian distribution. The power spectral density (PSD) of the two commonly used turbulence models, Dryden and von Kármán models are respectively given by [16]

$$\Phi_{Dw}(\omega) = \sigma^2 \frac{L_g}{\pi V} \frac{1 + 3(\frac{L_g \omega}{V})^2}{[1 + (\frac{L_g \omega}{V})^2]^2}, \quad \Phi_{vKw}(\omega) = \sigma^2 \frac{L_g}{\pi V} \frac{1 + \frac{8}{3}(a\frac{L_g \omega}{V})^2}{\left[1 + (a\frac{L_g \omega}{V})^2\right]^{\frac{11}{6}}} \tag{11}$$

where ω is the circular frequency, L_g is the turbulence scale length, σ is the turbulence intensity, constant $a = 1.339$, and V is the aircraft speed.

While von Kármán model better fits available experimental and theoretical data especially in high frequency range [17], its irrational spectra requires approximate difference equations to generate turbulence velocities in the time domain. As an alternative, the von Kármán spectrum can be realized in the spatial domain [13]. In this paper, the external disturbances are assumed to be symmetrical to the aircraft (O_f, x_f, y_f) plane, while the turbulence velocities vary along the wing span. For example, a realization of the 2D symmetrical von Kármán moderate turbulence field with $L_g = 762\ m$ and $\sigma = 1.5\ m/s$ is shown in Fig. 2.

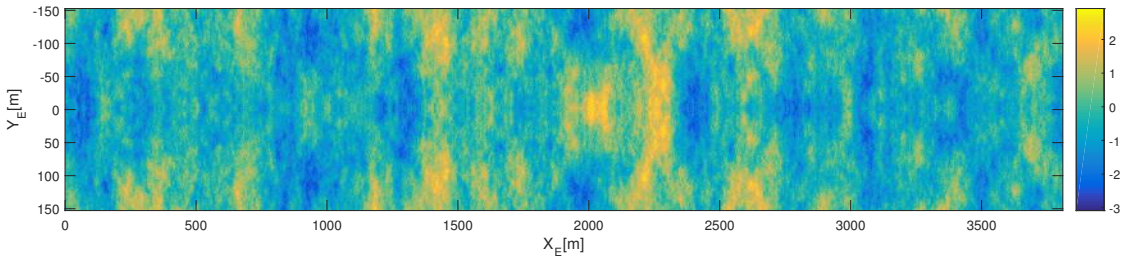

Fig. 2 A 2D symmetrical von Kármán vertical turbulence field ($L_g = 762$m, $\sigma = 1.5$ m/s).

The rational spectra of Dryden model allows it to be realized in the time domain by passing a white noise through a filter given by Eq. (12). This filter will be used in the state estimation process.

$$H_{Dw}(s) = \sigma \sqrt{\frac{L_g}{\pi V}} \frac{1 + \frac{\sqrt{3} L_g}{V} s}{(1 + \frac{L_g}{V} s)^2} \tag{12}$$

The "1-cos" gust model can more precisely capture the solitary gust feature compared to sharp-edged and ramped gust models. A "1-cos" gust is defined as Eq. (13) and can be broadened into symmetric w_{g_s} and asymmetric w_{g_a} gust field as described by Eq. (14).

$$w_g = \frac{w_m}{2}(1 - \cos\frac{2\pi X_E}{\lambda_x}), \tag{13}$$

$$w_{g_s} = \frac{w_m}{4}(1 - \cos\frac{2\pi X_E}{\lambda_x})(1 - \cos\frac{2\pi Y_E}{\lambda_y}), \qquad w_{g_a} = \frac{w_m}{2}(1 - \cos\frac{2\pi X_E}{\lambda_x})\sin\frac{2\pi Y_E}{\lambda_y} \tag{14}$$

where w_m represents the maximum gust velocity and λ_x, λ_y refer to the gust lengths in X_E, Y_E directions. An example of variant symmetric gust field is given in Fig. 3, in which the parameters of the first gust peak w_{g_1} is $\lambda_{x_1} = \lambda_{y_1} = 100$ m, $w_{m_1} = 5$ m/s and of the second gust peak w_{g_2} is $\lambda_{x_2} = \lambda_{y_2} = 180$ m, $w_{m_2} = 5$ m/s.

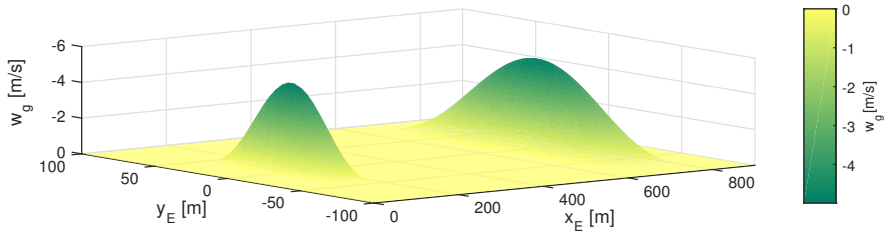

Fig. 3 2D symmetrical "1-cos" vertical gust field.

During simulations, the flexible aircraft is flying through 2D spatial turbulence and gust fields gradually. Since the gust induced velocities are different for each strip, the gust penetration effect is naturally captured.

III. INDI Control of the Flexible Aircraft

A. INDI GLA Control Law

The Incremental Nonlinear Dynamic Inversion (INDI) is a nonlinear control method, which improves the robust performance of the closed-loop system by making full use of sensor measurements. Expand the generalized nonlinear system dynamic equation into the first order Taylor series expansion around the current states and control inputs (denoted by subscript 0) to obtain an incremental form as

$$\dot{\boldsymbol{x}} = \boldsymbol{f}(\boldsymbol{x}) + \boldsymbol{g}(\boldsymbol{x}, \boldsymbol{u}) = \dot{\boldsymbol{x}}_0 + (\frac{\partial \boldsymbol{f}}{\partial \boldsymbol{x}}\Big|_0 + \frac{\partial \boldsymbol{g}}{\partial \boldsymbol{x}}\Big|_0)\Delta\boldsymbol{x} + \frac{\partial \boldsymbol{g}}{\partial \boldsymbol{u}}\Big|_0 \Delta\boldsymbol{u} + O(\Delta\boldsymbol{x}^2, \Delta\boldsymbol{u}^2) \tag{15}$$

For rigid aircraft flight control problems, the state variation $\Delta\boldsymbol{x}$ related terms and the higher-order linearization error $O(\Delta\boldsymbol{x}^2, \Delta\boldsymbol{u}^2)$ in Eq. (15) can be omitted based on the time scale separation principle [11–15]. For rigid aircraft, this principle means that the control surface deflections directly change the aerodynamic forces and moments, leading to the variations of angular and linear accelerations as direct effects. Following this, the changes in sates will gradually accumulate over time. Hence, when the sampling frequency is high, the state variation related terms are negligible. Define the control effectiveness matrix as $G = \frac{\partial \boldsymbol{g}}{\partial \boldsymbol{u}}\big|_0$, the incremental control input is calculated by inverting Eq. (15) as $\Delta\boldsymbol{u} = G^{-1}(\boldsymbol{\nu} - \dot{\boldsymbol{x}}_0)$. $\boldsymbol{\nu}$ is the virtual control (or pseudo-control), which can be designed by the outer-loop linear controllers [11–15]. The main feature of INDI control is its inherent robustness to model uncertainties. The incremental control law is independent of the model information of $\boldsymbol{f}(\boldsymbol{x})$, and the major part of model dynamics can be reflected by sensor measurements $\dot{\boldsymbol{x}}_0$, $\boldsymbol{x}_0$. The robustness of this controller for rigid aircraft applications has been demonstrated in [11–15].

In this section, the INDI GLA control law will be designed for flexible aircraft. The external disturbances (e.g. turbulence and gust) are viewed as perturbations to the nominal system, and will be considered in the pseudo-control design. For the nominal system without perturbation, define the rigid-body states as $\boldsymbol{x}_r = [\boldsymbol{V}_f^T \ \boldsymbol{\omega}_f^T]^T$, and the elastic states as $\boldsymbol{x}_e = [\boldsymbol{q}^T \ \boldsymbol{\xi}^T]^T$. Expand the dynamic part of Eq. (9) into the

incremental form and omit the higher-order terms as

$$
\begin{aligned}
\dot{\mathbf{p}}_{V_f} &= \dot{\mathbf{p}}_{V_{f_0}} + (-\frac{\partial \tilde{\omega}_f \mathbf{p}_{V_f}}{\partial \boldsymbol{x}_r}\Big|_0 \Delta \boldsymbol{x}_r - \frac{\partial \tilde{\omega}_f \mathbf{p}_{V_f}}{\partial \dot{\boldsymbol{x}}_e}\Big|_0 \Delta \dot{\boldsymbol{x}}_e + \frac{\partial \mathbf{F}}{\partial \boldsymbol{x}_r}\Big|_0 \Delta \boldsymbol{x}_r) + \frac{\partial \mathbf{F}}{\partial \boldsymbol{x}_e}\Big|_0 \Delta \boldsymbol{x}_e + \frac{\partial \mathbf{F}}{\partial \dot{\boldsymbol{x}}_e}\Big|_0 \Delta \dot{\boldsymbol{x}}_e \\
&\quad + \frac{\partial \mathbf{F}}{\partial \boldsymbol{u}}\Big|_0 \Delta \boldsymbol{u} \triangleq \dot{\mathbf{p}}_{V_{f_0}} + \mathbf{K}_r + \mathbf{K}_e + \mathbf{K}_{de} + \mathbf{K}_u \\
\dot{\mathbf{p}}_{\omega_f} &= \dot{\mathbf{p}}_{\omega_{f_0}} + (-\frac{\partial \tilde{V}_f \mathbf{p}_{V_f} + \tilde{\omega}_f \mathbf{p}_{\omega_f}}{\partial \boldsymbol{x}_r}\Big|_0 \Delta \boldsymbol{x}_r - \frac{\partial \tilde{V}_f \mathbf{p}_{V_f} + \tilde{\omega}_f \mathbf{p}_{\omega_f}}{\partial \dot{\boldsymbol{x}}_e}\Big|_0 \Delta \dot{\boldsymbol{x}}_e + \frac{\partial \mathbf{M}}{\partial \boldsymbol{x}_r}\Big|_0 \Delta \boldsymbol{x}_r) \\
&\quad + \frac{\partial \mathbf{M}}{\partial \boldsymbol{x}_e}\Big|_0 \Delta \boldsymbol{x}_e + \frac{\partial \mathbf{M}}{\partial \dot{\boldsymbol{x}}_e}\Big|_0 \Delta \dot{\boldsymbol{x}}_e + \frac{\partial \mathbf{M}}{\partial \boldsymbol{u}}\Big|_0 \Delta \boldsymbol{u} \triangleq \dot{\mathbf{p}}_{\omega_{f_0}} + \mathbf{W}_r + \mathbf{W}_e + \mathbf{W}_{de} + \mathbf{W}_u \\
\dot{\mathbf{p}}_{uw} &= \dot{\mathbf{p}}_{uw_0} - \mathcal{K}_{uw} \Delta \boldsymbol{q} - C_{uw} \Delta \boldsymbol{s} + (\frac{\partial \boldsymbol{Q}}{\partial \boldsymbol{x}_r}\Big|_0 \Delta \boldsymbol{x}_r + \frac{\partial (\frac{\partial \mathcal{T}}{\partial \boldsymbol{q}})}{\partial \boldsymbol{x}_r}\Big|_0 \Delta \boldsymbol{x}_r + \frac{\partial (\frac{\partial \mathcal{T}}{\partial \boldsymbol{q}})}{\partial \boldsymbol{x}_e}\Big|_0 \Delta \boldsymbol{x}_e + \frac{\partial (\frac{\partial \mathcal{T}}{\partial \boldsymbol{q}})}{\partial \dot{\boldsymbol{x}}_e}\Big|_0 \Delta \dot{\boldsymbol{x}}_e) \\
&\quad + \frac{\partial \boldsymbol{Q}}{\partial \boldsymbol{x}_e}\Big|_0 \Delta \boldsymbol{x}_e + \frac{\partial \boldsymbol{Q}}{\partial \dot{\boldsymbol{x}}_e}\Big|_0 \Delta \dot{\boldsymbol{x}}_e + \frac{\partial \boldsymbol{Q}}{\partial \boldsymbol{u}}\Big|_0 \Delta \boldsymbol{u} \triangleq \dot{\mathbf{p}}_{uw_0} + \mathbf{U}_q + \mathbf{U}_s + \mathbf{U}_r + \mathbf{U}_e + \mathbf{U}_{de} + \mathbf{U}_u \\
\dot{\mathbf{p}}_{\psi w} &= \dot{\mathbf{p}}_{\psi w_0} - \mathcal{K}_{\psi w} \Delta \boldsymbol{\xi} - C_{\psi w} \Delta \boldsymbol{\eta} + \frac{\partial \boldsymbol{\Theta}}{\partial \boldsymbol{x}_r}\Big|_0 \Delta \boldsymbol{x}_r + \frac{\partial \boldsymbol{\Theta}}{\partial \boldsymbol{x}_e}\Big|_0 \Delta \boldsymbol{x}_e + \frac{\partial \boldsymbol{\Theta}}{\partial \dot{\boldsymbol{x}}_e}\Big|_0 \Delta \dot{\boldsymbol{x}}_e + \frac{\partial \boldsymbol{\Theta}}{\partial \boldsymbol{u}}\Big|_0 \Delta \boldsymbol{u} \\
&\triangleq \dot{\mathbf{p}}_{\psi w_0} + \mathbf{Y}_\xi + \mathbf{Y}_\eta + \mathbf{Y}_r + \mathbf{Y}_e + \mathbf{Y}_{de} + \mathbf{Y}_u
\end{aligned} \tag{16}
$$

In the above equations, the control vector is given as $\boldsymbol{u} = [\delta_{a_s}, \delta_{a_a}, \delta_e, \delta_r]^T$. Since the throttle δ_p has low bandwidth, it is omitted from the INDI control loop. Throttle δ_p command is given by a separate proportional-integral controller to retain airspeed.

Eq. (16) can be simplified based on the time scale separation principle [11, 12, 15]. This principle for flexible aircraft can be redefined as: The control surface deflections will directly change the generalized forces $\mathbf{F}, \mathbf{M}, \boldsymbol{Q}, \boldsymbol{\Theta}$, leading to the changes of angular, linear, elastic accelerations as direct effects. The variations of the elastic deformation velocities and deformations are at comparable time scale. Nonetheless, the dynamics of the rigid-body states $\boldsymbol{x}_r = [\boldsymbol{V}_f^T \ \boldsymbol{\omega}_f^T]^T$ have larger time scale, so the variations of $\boldsymbol{x}_r$ can only gradually accumulate over time. In other words, when the sampling frequency is high, in one incremental time step, the $\Delta \boldsymbol{x}_r$ related terms can be neglected.

Because the off-diagonal elements of the mass matrix are relatively small, when the aircraft experiencing moderate maneuvers, the partial derivatives of the nonlinear terms in the translational and rotational equations with respect to $\dot{\boldsymbol{x}}_e$ can also be omitted in Δt.

The partial derivatives of the Coriolis and centrifugal forces with respect to $\boldsymbol{x}_e$ and $\dot{\boldsymbol{x}}_e$ are

$$
\frac{\partial (\frac{\partial \mathcal{T}}{\partial \boldsymbol{q}})}{\partial \boldsymbol{q}} = m_w \Phi \widetilde{C_w \omega_f}^T \widetilde{C_w \omega_f} \Phi, \quad \frac{\partial (\frac{\partial \mathcal{T}}{\partial \boldsymbol{q}})}{\partial \boldsymbol{s}} = m_w \Phi \widetilde{C_w \omega_f}^T \Phi, \quad \frac{\partial (\frac{\partial \mathcal{T}}{\partial \boldsymbol{q}})}{\partial \boldsymbol{\xi}} = \mathbf{0}, \quad \frac{\partial (\frac{\partial \mathcal{T}}{\partial \boldsymbol{q}})}{\partial \boldsymbol{\eta}} = \Phi \widetilde{C_w \omega_f}^T \int \tilde{r}_w \Psi dm_w \tag{17}
$$

The influences of these terms on bending deformations are negligible for small dihedral wing aircraft experiencing moderate maneuvers. For simplicity, the incremental terms in the translational, rotational, bending and torsion dynamic equations are respectively denoted by $\mathbf{K}, \mathbf{W}, \mathbf{U}, \mathbf{Y}$, whose values will be numerically compared term by term in the Sec. IV. Based on the above analyses, in one incremental time

step, the $\mathbf{K}_r, \mathbf{W}_r, \mathbf{U}_r, \mathbf{Y}_r$ terms can be eliminated. Eq. (16) can then be simplified into the following form

$$\begin{bmatrix} \dot{\mathbf{p}}_{V_f} \\ \dot{\mathbf{p}}_{\omega_f} \\ \dot{\mathbf{p}}_{uw} \\ \dot{\mathbf{p}}_{\psi w} \\ \dot{\boldsymbol{q}} \\ \dot{\boldsymbol{\xi}} \end{bmatrix} = \begin{bmatrix} \dot{\mathbf{p}}_{V_{f_0}} \\ \dot{\mathbf{p}}_{\omega_{f_0}} \\ \dot{\mathbf{p}}_{uw_0} \\ \dot{\mathbf{p}}_{\psi w_0} \\ \dot{\boldsymbol{q}}_0 \\ \dot{\boldsymbol{\xi}}_0 \end{bmatrix} + \left[\begin{array}{c|cc|cc} \mathbf{0} & \frac{\partial \mathbf{F}}{\partial \boldsymbol{s}} & \frac{\partial \mathbf{F}}{\partial \boldsymbol{\eta}} & \frac{\partial \mathbf{F}}{\partial \boldsymbol{q}} & \frac{\partial \mathbf{F}}{\partial \boldsymbol{\xi}} \\ & \frac{\partial \mathbf{M}}{\partial \boldsymbol{s}} & \frac{\partial \mathbf{M}}{\partial \boldsymbol{\eta}} & \frac{\partial \mathbf{M}}{\partial \boldsymbol{q}} & \frac{\partial \mathbf{M}}{\partial \boldsymbol{\xi}} \\ \mathbf{0} & -C_{uw} + \frac{\partial \boldsymbol{Q}}{\partial \boldsymbol{s}} & \frac{\partial \boldsymbol{Q}}{\partial \boldsymbol{\eta}} & -\mathcal{K}_{uw} + \frac{\partial \boldsymbol{Q}}{\partial \boldsymbol{q}} & \frac{\partial \boldsymbol{Q}}{\partial \boldsymbol{\xi}} \\ & \frac{\partial \boldsymbol{\Theta}}{\partial \boldsymbol{s}} & -C_{\psi w} + \frac{\partial \boldsymbol{\Theta}}{\partial \boldsymbol{\eta}} & \frac{\partial \boldsymbol{\Theta}}{\partial \boldsymbol{q}} & -\mathcal{K}_{\psi w} + \frac{\partial \boldsymbol{\Theta}}{\partial \boldsymbol{\xi}} \\ \mathbf{0} & \boldsymbol{I} & & \mathbf{0} & \end{array} \right]\Bigg|_0 \begin{bmatrix} \Delta \boldsymbol{V}_f \\ \Delta \boldsymbol{\omega}_f \\ \Delta \boldsymbol{s} \\ \Delta \boldsymbol{\eta} \\ \Delta \boldsymbol{q} \\ \Delta \boldsymbol{\xi} \end{bmatrix}$$

$$+ \left[\begin{array}{cc|c} \frac{\partial \mathbf{F}}{\partial \delta_{a_s}} & \frac{\partial \mathbf{F}}{\partial \delta_{a_a}} & \frac{\partial \mathbf{F}}{\partial \delta_e} \quad \frac{\partial \mathbf{F}}{\partial \delta_r} \\ \frac{\partial \mathbf{M}}{\partial \delta_{a_s}} & \frac{\partial \mathbf{M}}{\partial \delta_{a_a}} & \frac{\partial \mathbf{M}}{\partial \delta_e} \quad \frac{\partial \mathbf{M}}{\partial \delta_r} \\ \frac{\partial \boldsymbol{Q}}{\partial \delta_{a_s}} & \frac{\partial \boldsymbol{Q}}{\partial \delta_{a_a}} & \\ \frac{\partial \boldsymbol{\Theta}}{\partial \delta_{a_s}} & \frac{\partial \boldsymbol{\Theta}}{\partial \delta_{a_a}} & \mathbf{0} \\ & & \\ \mathbf{0} & & \mathbf{0} \end{array} \right]\Bigg|_0 \begin{bmatrix} \Delta \delta_{a_s} \\ \Delta \delta_{a_a} \\ \Delta \delta_e \\ \Delta \delta_r \end{bmatrix} \tag{18}$$

where $\boldsymbol{I}$ and $\mathbf{0}$ are identity matrix and zero matrix. In view of Eq. (18), the partial derivatives of the generalized forces with respect to $\boldsymbol{x}_e$ and $\dot{\boldsymbol{x}}_e$ contribute to aerodynamic stiffness and damping respectively. Besides, the control surface deflections directly lead to acceleration variations.

The state vector is defined as $\boldsymbol{x} = [\mathbf{p}_{V_f}^T \ \mathbf{p}_{\omega_f}^T \ \mathbf{p}_{uw}^T \ \mathbf{p}_{\psi w}^T \ \boldsymbol{q}^T \ \boldsymbol{\xi}^T]^T$ for the convenience of the virtual control design. Velocities and deformations can also be used as states as $\boldsymbol{x}_V = [\boldsymbol{V}_f^T \ \boldsymbol{\omega}_f^T \ \boldsymbol{s}^T \ \boldsymbol{\eta}^T \ \boldsymbol{q}^T \ \boldsymbol{\xi}^T]^T$, with a simple transformation of $\boldsymbol{x} = M_s \boldsymbol{x}_V, M_s = \mathrm{diag}([M, \boldsymbol{I}])$. Recall Eq. (18), the system dynamic equation can be written as

$$\dot{\boldsymbol{x}} = \dot{\boldsymbol{x}}_0 + \Gamma\big|_0 \Delta \boldsymbol{x}_V + \Upsilon\big|_0 \Delta \boldsymbol{u} = \dot{\boldsymbol{x}}_0 + (\Gamma M_s^{-1})\big|_0 \Delta \boldsymbol{x} + \Upsilon\big|_0 \Delta \boldsymbol{u} \tag{19}$$

The above equation is different from the incremental dynamic equation for rigid aircraft [11–15] since $\Delta \boldsymbol{x}$ related term still remains. Denote $A_e \triangleq (\Gamma M_s^{-1})|_0$, $B_e \triangleq \Upsilon|_0$, Eq. (18) is rewritten as

$$\dot{\boldsymbol{x}} = \dot{\boldsymbol{x}}_0 + A_e \Delta \boldsymbol{x} + B_e \Delta \boldsymbol{u} \tag{20}$$

The main control aim of this paper is load alleviation, so a reference model is designed to generate references for the states and state derivatives for load control purposes. Loads are caused by external forces and moments, and are perturbed by atmospheric disturbances. The strategy of this controller is to use control surface deflections to compensate for the load variations, so that the total forces and moments are retained at their nominal values $\mathbf{F}_*, \mathbf{M}_*, \boldsymbol{Q}_*, \boldsymbol{\Theta}_*$. Expand the total force as the nominal force $\mathbf{F}_*$, the forces variations due to aerodynamic uncertainties $\Delta \mathbf{F}_a$, caused by atmospheric disturbances $\Delta \mathbf{F}_d$, and generated by control inputs $\Delta \mathbf{F}_c$ as

$$\mathbf{F} = \mathbf{F}_* + \Delta \mathbf{F}_a + \Delta \mathbf{F}_d + \Delta \mathbf{F}_c \tag{21}$$

The moment $\mathbf{M}$, and generalized elastic forces $\boldsymbol{Q}$ and $\boldsymbol{\Theta}$ can also be expanded in this form. In order to retain the forces and moments at their nominal values, the desired forces generated by the control surfaces should be

$$\begin{aligned} \Delta \mathbf{F}_c &= -\Delta(\mathbf{F}_a + \mathbf{F}_d), \quad \Delta \mathbf{M}_c = -\Delta(\mathbf{M}_a + \mathbf{M}_d) \\ \Delta \boldsymbol{Q}_c &= -\Delta(\boldsymbol{Q}_a + \boldsymbol{Q}_d), \quad \Delta \boldsymbol{\Theta}_c = -\Delta(\boldsymbol{\Theta}_a + \boldsymbol{\Theta}_d) \end{aligned} \tag{22}$$

Recall Eq. (9), in order to satisfy the above equations, the virtual control $\boldsymbol{\nu}_{rm} = [\boldsymbol{\nu}_{\mathbf{P}_{V_f}}^T \ \boldsymbol{\nu}_{\mathbf{P}_{\omega_f}}^T \ \boldsymbol{\nu}_{\mathbf{P}_{uw}}^T \ \boldsymbol{\nu}_{\mathbf{P}_{\psi w}}^T \ \boldsymbol{\nu}_{\boldsymbol{q}}^T \ \boldsymbol{\nu}_{\boldsymbol{\xi}}^T]^T$

can be designed as

$$\begin{aligned}
\boldsymbol{\nu}_{\mathbf{P}_{V_f}} &= -\tilde{\omega}_f \mathbf{p}_{V_f} + \mathbf{F}_* \\
\boldsymbol{\nu}_{\mathbf{P}_{\omega_f}} &= -\tilde{V}_f \mathbf{p}_{V_f} - \tilde{\omega}_f \mathbf{p}_{\omega_f} + \mathbf{M}_* \\
\boldsymbol{\nu}_{\mathbf{P}_{uw}} &= -\mathcal{K}_{uw}\boldsymbol{q} - C_{uw}\boldsymbol{s} + \boldsymbol{Q}_* = -\mathcal{K}_{uw}(\boldsymbol{q} - \boldsymbol{q}_*) - C_{uw}(\boldsymbol{s} - \boldsymbol{s}_*) \\
\boldsymbol{\nu}_{\mathbf{P}_{\psi w}} &= -\mathcal{K}_{\psi w}\boldsymbol{\xi} - C_{\psi w}\boldsymbol{\eta} + \boldsymbol{\Theta}_* = -\mathcal{K}_{\psi w}(\boldsymbol{\xi} - \boldsymbol{\xi}_*) - C_{\psi w}(\boldsymbol{\eta} - \boldsymbol{\eta}_*) \\
\boldsymbol{\nu}_{\boldsymbol{q}} &= \mathbf{0}, \quad \boldsymbol{\nu}_{\boldsymbol{\xi}} = \mathbf{0}
\end{aligned} \tag{23}$$

If the nominal condition is steady level flight, then $\mathbf{F}_* = \mathbf{M}_* = \boldsymbol{s}_* = \boldsymbol{\eta}_* = \mathbf{0}$. The nominal condition can also be constant speed climb and decent, level turn, etc. The desired $\dot{\boldsymbol{q}}$, $\dot{\boldsymbol{\xi}}$ are all equal to zero. The reference for states are obtained by integrating the virtual control as

$$\boldsymbol{x}_{rm} = \boldsymbol{x}_{rm_*} + \int_0^t \boldsymbol{\nu}_{rm} d\tau \tag{24}$$

A proportional virtual control term $\boldsymbol{\nu}_p$ is added to minimize the reference tracking errors as

$$\boldsymbol{\nu} = \boldsymbol{\nu}_{rm} + \boldsymbol{\nu}_p = \boldsymbol{\nu}_{rm} + K_p(\boldsymbol{x}_{rm} - \boldsymbol{x}_0) \tag{25}$$

where K_p is a positive definite diagonal matrix. The incremental control input is designed by replacing $\dot{\boldsymbol{x}}$ and $\boldsymbol{x}$ in Eq. (20) by their desired values $\boldsymbol{\nu}$ and $\boldsymbol{x}_{rm}$, and then inverting Eq. (20) as

$$\begin{aligned}
(\boldsymbol{\nu} - \dot{\boldsymbol{x}}_0) - A_e(\boldsymbol{x}_{rm} - \boldsymbol{x}_0) &= B_e \Delta \boldsymbol{u} \\
\Delta \boldsymbol{u} &= (B_e^T W B_e)^{-1} B_e^T W[(\boldsymbol{\nu} - \dot{\boldsymbol{x}}_0) - A_e(\boldsymbol{x}_{rm} - \boldsymbol{x}_0)]
\end{aligned} \tag{26}$$

For the reason that the number of control variable is less than the number of states, the weighted least squares method is used in the present INDI control law. The weighting matrix W is chosen as a positive definite diagonal matrix, and can be tuned based on the control priority. The complete INDI GLA control law structure is illustrated by Fig. 4, where $A(s)$ and $A_p(s)$ represent the actuator dynamics of the control surfaces and throttle respectively.

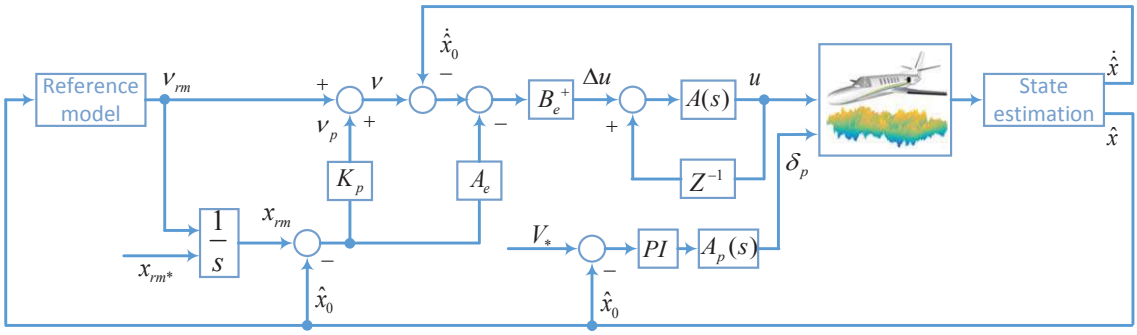

Fig. 4 Flexible aircraft INDI gust load alleviation control law structure.

B. Sensing and State Estimation

The INDI GLA control law designed by Eqs. (23, 26) requires the feedback of the states $\boldsymbol{x}_0$ and states derivatives $\dot{\boldsymbol{x}}_0$. Rigid-body states $\boldsymbol{x}_r = [\boldsymbol{V}_f^T \ \boldsymbol{\omega}_f^T]^T$ and $\dot{\boldsymbol{V}}_f$ can be obtained from integrated inertial navigation system. Angular accelerations can be measured directly by angular accelerometers, numerically differentiated from gyro measurements [15], predicted by a linear predictive filter [11], etc.

The aeroelastic state vector $\boldsymbol{x}_e = [\boldsymbol{q}^T \ \boldsymbol{\xi}^T]^T$ is generally not accessible, but can be estimated using an observer, which is a standard control practice. Nine accelerometers are placed on the flexible aircraft to capture the wing bending and torsion motions. One accelerometer is installed on the c.g. and four

accelerometers are placed on each wing as shown by the red dots in Fig. 1. At each wing, the accelerometers are placed in pairs at the mid-span and the wing tip. For each pair, one accelerometer is placed in front of the elastic axis, and the other one is behind, so that the torsion movements can be observed.

The wing accelerometer outputs can be modeled by considering an infinitesimal mass element *dm* on the wing, whose absolute acceleration can be calculated by differentiating Eq. (3) as

$$\mathbf{a}_w(\mathbf{r}_w, t) = C_w\dot{\mathbf{V}}_f + C_w\tilde{r}_{fw}^T\dot{\boldsymbol{\omega}}_f + (\tilde{r}_w + \widetilde{\Phi \boldsymbol{q}})^T C_w\dot{\boldsymbol{\omega}}_f + \widetilde{\Phi \boldsymbol{s}}^T C_w\boldsymbol{\omega}_f + \tilde{r}_w^T\Psi\dot{\boldsymbol{\eta}} + \Phi\dot{\boldsymbol{s}} \tag{27}$$

Eq. (27) gives the accelerometer measurements. The system output equation can be written in the form of $\mathbf{y} = \boldsymbol{h}(\boldsymbol{x}) + \mathbf{v}$, where $\mathbf{v}$ is the measurement noise.

The Extended Kalman Filter (EKF) and Unscented Kalman Filter (UKF) are widely used for state estimation of nonlinear systems, which however require high computational power. In view of that the INDI control is able to retain the state near the equilibrium point, the linearization error is small for the closed-loop system. As a result, the linear Kalman Filter (KF) is a reasonable and efficient observer for online state estimations. The linearized system dynamics can be written as

$$\begin{aligned}
\begin{bmatrix} \dot{\boldsymbol{x}}_r \\ \ddot{\boldsymbol{x}}_e \\ \dot{\boldsymbol{x}}_e \end{bmatrix} &= \left[\begin{array}{c|cc} A_{rr} & A_{re} \\ \hline A_{er} & A_{ee} \end{array}\right] \begin{bmatrix} \boldsymbol{x}_r \\ \dot{\boldsymbol{x}}_e \\ \boldsymbol{x}_e \end{bmatrix} + \begin{bmatrix} B_r \\ \hline B_e \end{bmatrix} \boldsymbol{u} + \begin{bmatrix} \mathbf{w}_r \\ \hline \mathbf{w}_e \end{bmatrix} \\
\mathbf{y}_V &= \left[\begin{array}{c|cc} C_r & C_e \end{array}\right] \left[\begin{array}{c|cc} \boldsymbol{x}_r & \dot{\boldsymbol{x}}_e & \boldsymbol{x}_e \end{array}\right]^T + D_V\boldsymbol{u} + \mathbf{v}
\end{aligned} \tag{28}$$

The process noise $[\mathbf{w}_r^T \ \mathbf{w}_e^T]^T$ contains the model errors and external disturbances. For GLA problems, it is common to augment linear system models with Dryden turbulence model as a prior knowledge of the process noise [6, 18]. In reality, however, the turbulence spectrum is unpredictable. In order to get a satisfactory state estimation while making the controller be capable of handling a broad range of disturbances, the Dryden model is augmented into the system model with parametric uncertainties. These uncertain parameters can be modeled as random walks and estimated online. Recalling Eq. (12), the state-space realization of the Dryden spectrum can be given by

$$\begin{aligned}
\dot{\boldsymbol{x}}_w &= A_w\boldsymbol{x}_w + B_w\mathbf{n} \\
\mathbf{w}_{g_w} &= C_w\boldsymbol{x}_w
\end{aligned} \tag{29}$$

where $\mathbf{n}$ is Gaussian white noise. Regarding the linear model used for state estimation purposes, the gust penetration effect is roughly modeled as a time shift ς from the wing to the tail, and the gust velocities are assumed to be unified on the wing $\mathbf{w}_{g_w}$ and the tail $\mathbf{w}_{g_H}$. In other words, $\mathbf{w}_{g_H} = e^{-\varsigma s}\mathbf{w}_{g_w}$. The pure time delay $e^{-\varsigma s}$ is approximated using the fifth order Padé approximation in the Laplace domain, and can be realized in the time domain as

$$\begin{aligned}
\mathbf{w}_{g_H} &= e^{-\varsigma s}\mathbf{w}_{g_w} \approx H(\varsigma s)\mathbf{w}_{g_w} \\
\dot{\boldsymbol{x}}_\varsigma &= A_\varsigma\boldsymbol{x}_\varsigma + B_\varsigma\mathbf{w}_{g_w} = A_\varsigma\boldsymbol{x}_\varsigma + B_\varsigma C_w\boldsymbol{x}_w \\
\mathbf{w}_{g_H} &= C_\varsigma\boldsymbol{x}_\varsigma \\
\mathbf{w}_e &= E_w\mathbf{w}_{g_w} + E_H\mathbf{w}_{g_H} + \mathbf{d}
\end{aligned} \tag{30}$$

where $\mathbf{d}$ represents the aircraft and turbulence model errors. Since the rigid states $\boldsymbol{x}_r$ can be measured, they are treated as inputs to the elastic state estimation equation. In summary, the integrated linear model for Kalman filter estimation is written as

$$\begin{aligned}
\begin{bmatrix} \ddot{\boldsymbol{x}}_e \\ \dot{\boldsymbol{x}}_e \\ \dot{\boldsymbol{x}}_w \\ \dot{\boldsymbol{x}}_\varsigma \end{bmatrix} &= \left[\begin{array}{c|cc} A_{ee} & E_wC_w & E_HC_\varsigma \\ \hline 0 & A_w & 0 \\ 0 & B_\varsigma C_w & A_\varsigma \end{array}\right] \begin{bmatrix} \dot{\boldsymbol{x}}_e \\ \boldsymbol{x}_e \\ \boldsymbol{x}_w \\ \boldsymbol{x}_\varsigma \end{bmatrix} + \left[\begin{array}{c|c} B_e & A_{er} \\ \hline 0 & 0 \\ 0 & 0 \end{array}\right] \begin{bmatrix} \boldsymbol{u} \\ \hline \boldsymbol{x}_r \end{bmatrix} + \begin{bmatrix} 0 \\ \hline B_w \\ 0 \end{bmatrix} \mathbf{n} + \begin{bmatrix} \mathbf{d} \\ \hline 0 \\ 0 \end{bmatrix} \\
\mathbf{y}_V &= \left[\begin{array}{c|cc} C_e & 0 & 0 \end{array}\right] \left[\begin{array}{c|cc} \dot{\boldsymbol{x}}_e & \boldsymbol{x}_e & \boldsymbol{x}_w & \boldsymbol{x}_\varsigma \end{array}\right]^T + \left[\begin{array}{c|c} D_V & C_r \end{array}\right] \left[\begin{array}{c|c} \boldsymbol{u} & \boldsymbol{x}_r \end{array}\right]^T + \mathbf{v}
\end{aligned} \tag{31}$$

This linear model can be written in the form of

$$\begin{aligned} \dot{\boldsymbol{x}}_{kf} &= A_{kf}\boldsymbol{x}_{kf} + B_{kf}\boldsymbol{u}_{kf} + G_{kf}\mathbf{n} + \mathbf{d}_{kf} \\ \mathbf{y}_{kf} &= C_{kf}\boldsymbol{x}_{kf} + D_{kf}\boldsymbol{u}_{kf} + \mathbf{v} \end{aligned} \tag{32}$$

The observability matrix of this system is give by $O_\Gamma = [C_{kf}; C_{kf}A_{kf}; ...; C_{kf}A_{kf}^{n-1}]$, $\text{rank}(A_{kf}) = n$. For the present aircraft model, O_Γ is of full rank, which indicates this augmented system is fully observable. Eq. (32) can then be used for Kalman filter online estimation. The measurement noise covariance matrix is $R_{kf} = E\{\mathbf{v}\mathbf{v}^T\}$, and is set based on the realistic noise values for the accelerometers.

The process noise covariance matrix is chosen as $Q_{kf} = E\{G_{kf}\mathbf{n}\mathbf{n}^T G_{kf}^T\} + Q_d$, where Q_d is an additive matrix tuned to account for the aircraft and turbulence model errors. The effectiveness of this state estimation approach will be shown in Sec. IV.

IV. Simulation Results

The fully flexible aircraft model in [2] is simplified into a flexible-wing aircraft model in the present paper. The first two eigenfunctions of uniform cantilever beam and uniform clamped-free shaft are used as bending shape functions $\Phi(\mathbf{r}_w)$ and torsion shape functions $\Psi(\mathbf{r}_w)$ respectively. The geometry parameters, lumped form inertia properties, and local aerodynamic coefficients all adopt data from [2].

The sampling frequency of simulations is $f_s = 1000$ Hz. The throttle dynamics is model as a first order system with bandwidth 6 rad/s. All the control surface actuator dynamics are modeled as first order systems with transfer function $A(s) = \frac{20}{s+20}$. The deflection limits of ailerons, elevator and rudder are $\pm 30°, \pm 20°, \pm 20°$ respectively. The rate limits for ailerons are $100°/\text{s}$ and are $60°/\text{s}$ for elevator and rudder.

A. Flexible-Wing Aircraft Trimming

This flexible-wing aircraft model can be degraded into a quasi-rigid aircraft model [13], namely all the elastic deformations and deformation velocities are zero. This quasi-rigid aircraft model is compared with the present flexible aircraft model to indicate the couplings between structural and flight dynamics. Both the flexible aircraft and quasi-rigid aircraft are trimmed at steady level flight condition, with $H_* = 25000$ ft, $V_{E_*} = 127$ m/s, $Ma_* = 0.41$. The steady level flight trim constrains are given by

$$\begin{aligned} \dot{\boldsymbol{R}}_{f_*} &= [V_{E_*}\ 0\ 0]^T,\ \ \boldsymbol{\theta}_{f_*} = [0\ \theta_*\ 0]^T,\ \ \mathbf{V}_{f_*} = C_f(\boldsymbol{\theta}_*)\dot{\boldsymbol{R}}_{f_*}, \\ \boldsymbol{\omega}_{f_*} &= \mathbf{0},\ \ \alpha_* = \theta_*,\ \ \beta_* = 0,\ \ \boldsymbol{s}_* = \mathbf{0},\ \ \boldsymbol{\eta}_* = \mathbf{0} \end{aligned} \tag{33}$$

In view of the symmetric character of the steady level flight condition, asymmetric states and control inputs are automatically set to be zero. The trim solution is calculated by numerically iterating Eq. (9) until Eq. (33) is satisfied. The thrust F_{E_*}, angle of attack α_*, elevator deflection δ_{e_*}, and generalized coordinates $\boldsymbol{q}_*, \boldsymbol{\xi}_*$ in trim condition are given by Table 1.

Table 1 Trim solutions for the flexible and the quasi-rigid aircraft.

	V_{E_*} [m/s]	F_{E_*} [lb]	δ_{e_*} [°]	α_* [°]	$\boldsymbol{q}_*$ [mm]	$\boldsymbol{\xi}_*$ [°]
Flexible	127	627.3	-3.61	3.98	$[-34.29, 3.63]^T$	$[0.1044, -0.0105]^T$
Quasi-Rigid	127	633.2	-3.71	4.03		

Since the wing elastic axis is modeled to be consistent with the unswept wing beam in this model, the bending and torsion modes are decoupled. In trim condition, the wing is bending upwards with nose-up torsion angle. The required angle of attack is smaller for the flexible aircraft as compared to the quasi-rigid aircraft because of the nose-up twist.

Fig. 5 shows the eigenvalues of both the flexible and quasi-rigid aircraft. It can be seen from the figure that except four zero poles (for X_E, Y_E, Z_E, ψ), the interactions between rigid and flexible dynamics make the rigid mode poles of the flexible aircraft deviate from the poles of the quasi-rigid aircraft.

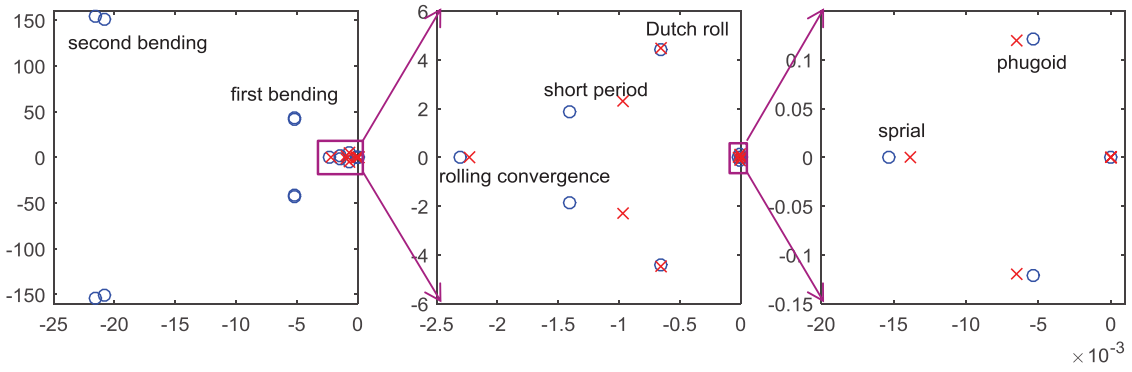

Fig. 5 Eigenvalues for flexible aircraft (blue circles) and quasi-rigid aircraft (red crosses).

B. Validation of the Time Scale Separation Principle

In Eq. (18), $\mathbf{K}_r, \mathbf{W}_r, \mathbf{U}_r, \mathbf{Y}_r$ terms are omitted for controller design. The $\Delta \boldsymbol{x}_r$ related terms are eliminated based on the physically explained time scale separation principle. For moderate maneuvers, the partial derivatives of the nonlinear cross coupling terms, the Coriolis and centrifugal forces with respect to $\boldsymbol{x}_e$ and $\dot{\boldsymbol{x}}_e$ can also be neglected. The term values in Eq. (16) will be numerically compared in this section.

The current condition (denoted by subscript 0) is taken as the trim point, and can be generalized into arbitrary time point during simulations. 1° step elevator δ_e, rudder δ_r, symmetric δ_{a_s} and asymmetric δ_{a_a} aileron deflection commands are given to the aircraft separately. In one incremental time step $\Delta t = 0.001$ s, the norm value of the terms are shown in Fig. 6. For simplicity, only the translational $\dot{\mathbf{P}}_{V_f}$, rotational $\dot{\mathbf{P}}_{\omega_f}$, right wing vibrations $\dot{\mathbf{P}}_{uwr}$ and $\dot{\mathbf{P}}_{\psi wr}$ are shown in the figure, and the left wing vibrations are exactly symmetrical or asymmetrical to the right.

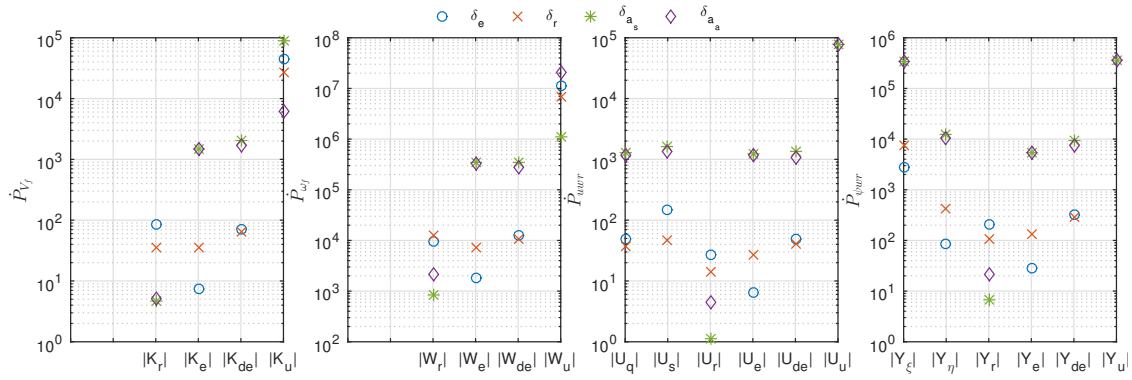

Fig. 6 Norm value of the terms in Eq. (16) in one incremental time step.

It can be seen from Fig. 6, the elevator (δ_e blue circles) and rudder (δ_r red cross) deflections directly lead to translational and rotational acceleration variations, because $\|\mathbf{K}_u\|$ and $\|\mathbf{W}_u\|$ are at least 2.5 orders of magnitude larger than $\|\mathbf{K}_r\|, \|\mathbf{K}_e\|, \|\mathbf{K}_{de}\|, \|\mathbf{W}_r\|, \|\mathbf{W}_e\|, \|\mathbf{W}_{de}\|$. δ_e and δ_a do not influence the generalized elastic forces $\boldsymbol{Q}$ and $\boldsymbol{\Theta}$ directly, so that $\|\mathbf{U}_u\| = \|\mathbf{Y}_u\| = 0$. Even so, the elevator and rudder deflections indirectly excite bending and torsion motions due to coupling effects, as $\|\mathbf{U}_q\|, \|\mathbf{U}_s\|, \|\mathbf{U}_r\|, \|\mathbf{U}_e\|, \|\mathbf{U}_{de}\|, \|\mathbf{Y}_\xi\|, \|\mathbf{Y}_\eta\|, \|\mathbf{Y}_r\|, \|\mathbf{Y}_e\|, \|\mathbf{Y}_{de}\|$ are nonzero.

The symmetric aileron (δ_{a_s} green asterisks) deflections directly lead to vertical translational ($\|\mathbf{K}_u\|$), bending ($\|\mathbf{U}_u\|$) and torsion ($\|\mathbf{Y}_u\|$) accelerations, as well as small pitching accelerations ($\|\mathbf{W}_u\|$). The variations of $\boldsymbol{x}_e$ and $\dot{\boldsymbol{x}}_e$ related terms are about 1.8, 0.5, 1.8 orders of magnitude smaller than $\boldsymbol{u}$ related terms in the translational, rotational, bending equations respectively. The torsion motion is in comparable time scale with acceleration variations, because of its higher frequency. This can be seen by comparing $\|\mathbf{Y}_\xi\|$

with $\|\mathbf{Y}_u\|$. Overall, under δ_{a_s} deflections, $\|\mathbf{K}_r\|$, $\|\mathbf{W}_r\|$, $\|\mathbf{U}_r\|$, $\|\mathbf{Y}_r\|$ are at least 2.5 orders of magnitude smaller than the remaining terms.

The term values under asymmetric aileron (δ_{a_a} purple diamonds) excitation show similar characters as under δ_{a_s} excitation. Namely the $\boldsymbol{x}_e$ and $\dot{\boldsymbol{x}}_e$ related terms have comparable variations as compared to $\boldsymbol{u}$ related terms, while $\|\mathbf{K}_r\|$, $\|\mathbf{W}_r\|$, $\|\mathbf{U}_r\|$, $\|\mathbf{Y}_r\|$ are at least 2 orders of magnitude smaller than the remaining terms.

The above simulation further verified the physically explained time scale separation principle for flexible aircraft.

C. State Estimation Results

The linear system model given by Eq. (32) is used to estimate the elastic states $\boldsymbol{x}_e$ and $\dot{\boldsymbol{x}}_e$ while the flexible aircraft is flying through a 2D symmetrical von Kámán turbulence field (Fig. 2). The parameters of the turbulence field are $L_g = 762$ m, $\sigma = 1.5$ m/s. The measurement noise $\mathbf{v}$ is modeled as white noise with standard deviation 0.03 m/s^2. The turbulence parameters used in the Dryden model are $L_g = 800$ m, $\sigma = 1.8$ m/s, which are chosen to be different from the actual turbulence field in order to model the turbulence model parametric uncertainties. As mentioned in Sec. III, these uncertain parameters can be modeled as random walk and estimated online. In this research, by tuning the process noise covariance matrix Q_{kf}, the Kalman filter already shows satisfactory results without directly estimating these uncertain parameters.

Fig. 7 illustrates the real and estimated elastic states $\boldsymbol{x}_e = [\boldsymbol{q}^T \ \boldsymbol{\xi}^T]^T$. As can be seen from Figs. 7, 8, the Kalman filter online estimation converges within 0.02 s. The estimation errors are all within the posterior estimate standard deviation boundary. Since the deformation velocities are more easily influenced by the disturbance, the estimated deformation velocities $\dot{\boldsymbol{x}}_e = [\boldsymbol{s}^T \ \boldsymbol{\eta}^T]^T$ present perceptible errors as shown in Fig. 9. One sigma of these errors remain in the posterior estimate standard deviation boundary as indicated in Fig. 10.

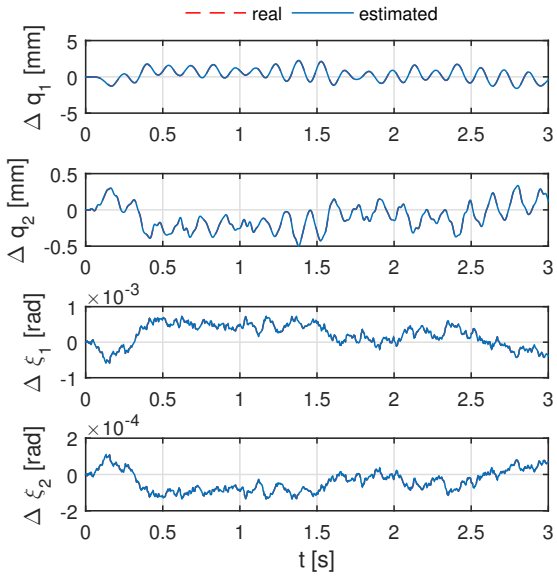

Fig. 7 Real and estimated deformations.

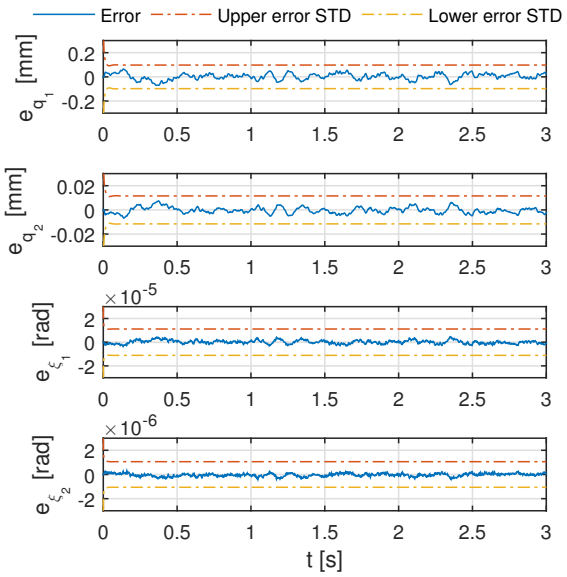

Fig. 8 Deformation estimation errors.

There are several ways of estimating the deformation accelerations $\ddot{\boldsymbol{x}}_e = [\dot{\boldsymbol{s}}^T \ \dot{\boldsymbol{\eta}}^T]^T$. $\ddot{\boldsymbol{x}}_e$ can be reconstructed from accelerometer measurements, this method however is sensitive to the structural vibrations. $\ddot{\boldsymbol{x}}_e$ can also be obtained by passing $\dot{\boldsymbol{x}}_e$ through the following washout filter [19]:

$$\frac{s\omega_n^2}{s^2 + 2\zeta_n\omega_n s + \omega_n^2} \tag{34}$$

with the estimation results shown in Fig. 11.

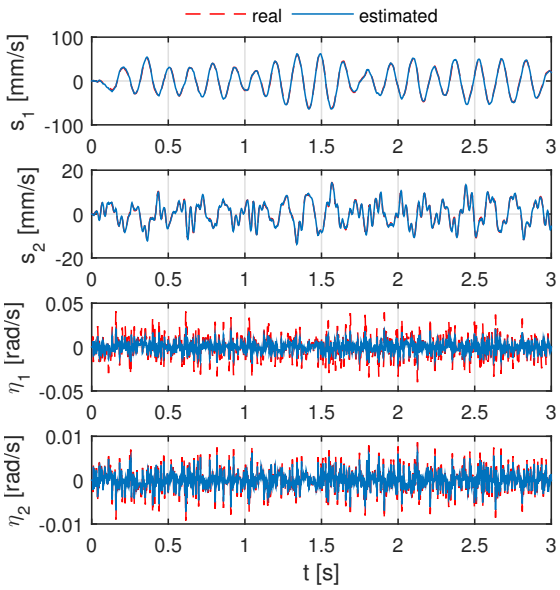

Fig. 9 Estimated deformation velocities.

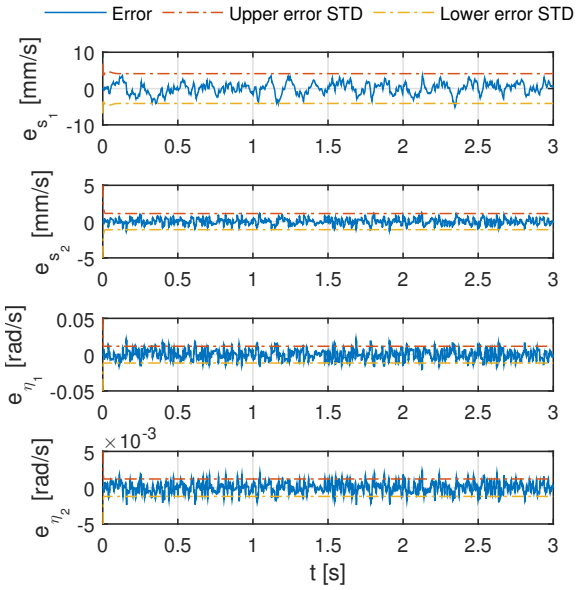

Fig. 10 Deformation velocity estimation errors.

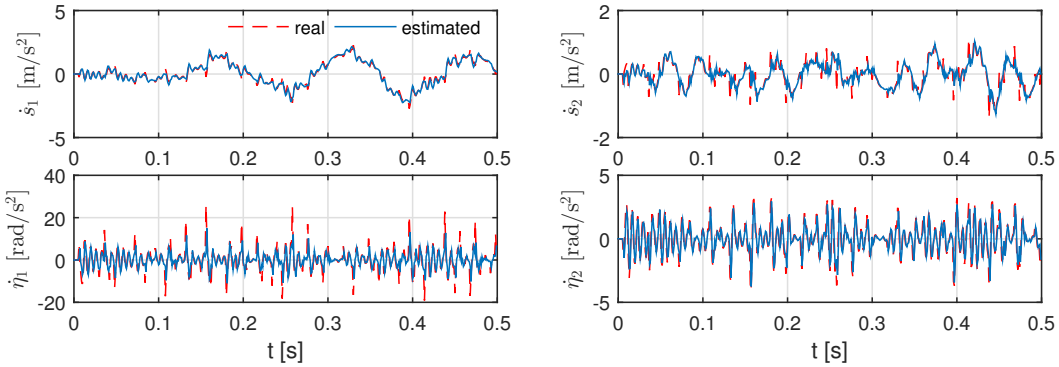

Fig. 11 Real and estimated wing deformation accelerations.

D. INDI GLA Simulation Results

In this section, the INDI GLA control law derived in Sec. III is applied on a flexible aircraft model flying through both a continuous turbulence field (Fig. 2) and discrete gust field (Fig. 3) to demonstrate its feasibility. Two major performance metrics are chosen as the deviation of vertical load and wing root bending moment from their trim values expressed as

$$\Delta n_z = n_z - n_{z_*}, \quad \Delta M_r = M_r - M_{r_*} \tag{35}$$

Figs. 12-15, illustrate the dynamic responses of the flexible aircraft flying through a von Kármán turbulence field (Fig. 2), in which "Open-loop" means responses without control. "INDI" means the closed-loop responses of the system under INDI GLA control, where the states $\boldsymbol{x}$ and their derivatives $\dot{\boldsymbol{x}}$ are assumed to be available. "INDI+KF" refers to the closed-loop system responses, in which the estimated $\hat{\boldsymbol{x}}$ and $\dot{\hat{\boldsymbol{x}}}$ are used by the controller. The RMS value as well as the peaks of Δn_z and ΔM_r are summarized in Table 2. It can be seen from Fig. 12 and Table 2 that the proposed INDI GLA controller effectively alleviated both the vertical load and the wing root bending moment. Since the state estimation is satisfactory, the closed-loop responses using estimated $\hat{\boldsymbol{x}}$ and $\dot{\hat{\boldsymbol{x}}}$ only have negligible deteriorations as compared to the ideal case where the real $\boldsymbol{x}$ and $\dot{\boldsymbol{x}}$ are used.

Fig. 13 shows the generalized elastic displacement responses, namely the first bending q_{r_1}, second bending q_{r_2}, and the first and second torsion ξ_{r_1} and ξ_{r_2} modes of the right wing. For this flexible aircraft configuration, only one set of aileron is available on the wing, which aims at wing bending and torsion modes suppression, vertical load control and roll rate control at the same time. However, according to the controllability analysis, this configuration is unable to achieve a decoupled control of all its missions. For example, in the presence of upwash gust, the wing lift increases, which results in load increment, upward bending and nose-up torsion of the wing as can be seen in Figs. 16-17. The symmetric up deflection of ailerons would alleviate the wing load and bending deformation, but would degrade the torsion deformation because the aerodynamic center of the aileron is behind the wing elastic axis. Since the torsion stiffness is normally larger than the bending stiffness, the vertical load and bending modes are weighted heavier in Eq. (26). As shown in Fig. 13, the bending modes of the flexible wing have been successfully suppressed, while the torsion deformations have reasonable increments. There are a couple of ways to improve the torsion responses. The fundamental solution would be adding control surfaces (e.g. inboard ailerons, flaperons, spoilers, etc.) to achieve a synergetic control with the outboard ailerons. Novel control surfaces like Variable Camber Continuous Trailing Edge Flap (VCCTEF) [20] are beneficial for elastic wing controls. Stiffening the wing box or increasing the control weights of the torsion motion are also possible approaches.

The pitch motions and velocity variations are also suppressed as shown in Fig. 14. The control inputs are illustrated in Fig. 15, the left aileron deflections δ_{al} is the same as the right δ_{ar} in the symmetric turbulence field.

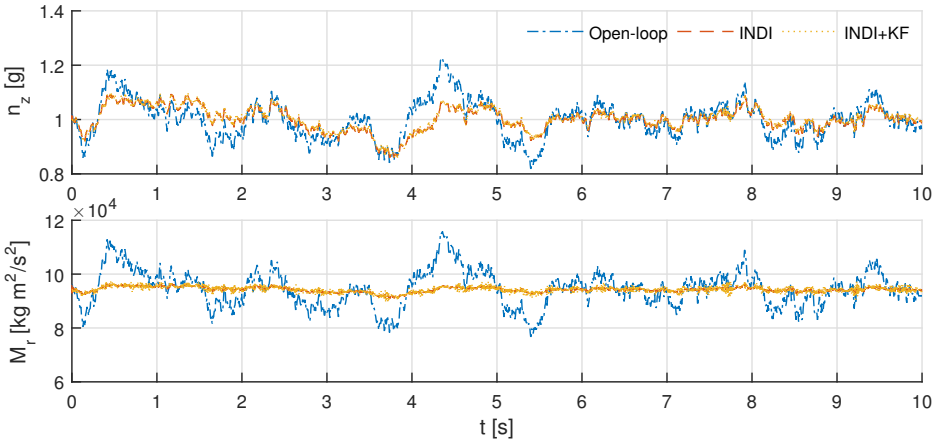

Fig. 12 Vertical load and wing root bending moment responses under turbulence excitation.

Table 2 The RMS, peaks of load and wing root bending moment increments under turbulence excitation.

	max $\lvert\Delta n_z\rvert$ [g]		$\hat{\sigma}_{\Delta n_z}$ [g]		max $\lvert\Delta M_r\rvert$ [kgm^2/s^2]		$\hat{\sigma}_{\Delta M_r}$ [kgm^2/s^2]	
Open-loop	0.2253		0.0691		2.17×10^4		6.73×10^3	
INDI	0.1397	38.0%	0.0432	37.5%	3.17×10^3	85.4%	922.7	86.3%
INDI+KF	0.1397	38.0%	0.0433	37.4%	4.74×10^3	78.1%	1.12×10^3	83.4%

The dynamic responses of the flexible aircraft in a symmetric "1-cos" gust field (Fig. 3) are illustrated in Figs. 16-18. As shown in Fig. 16 and Table 3. The vertical load and wing root bending moment have been alleviated by over 35% and 86% respectively. In the presence of upwash gusts, the ailerons deflect upward symmetrically to alleviate the wing load as shown in Fig. 19. Thrust and elevator are used to control the velocity and pitch motion as can be seen in Figs. 18-19. The generalized elastic displacements and wing tip deflections (Fig. 17) show analogous responses to the responses under turbulence excitation, namely the bending modes have been suppressed while the torsion motions have acceptable increments.

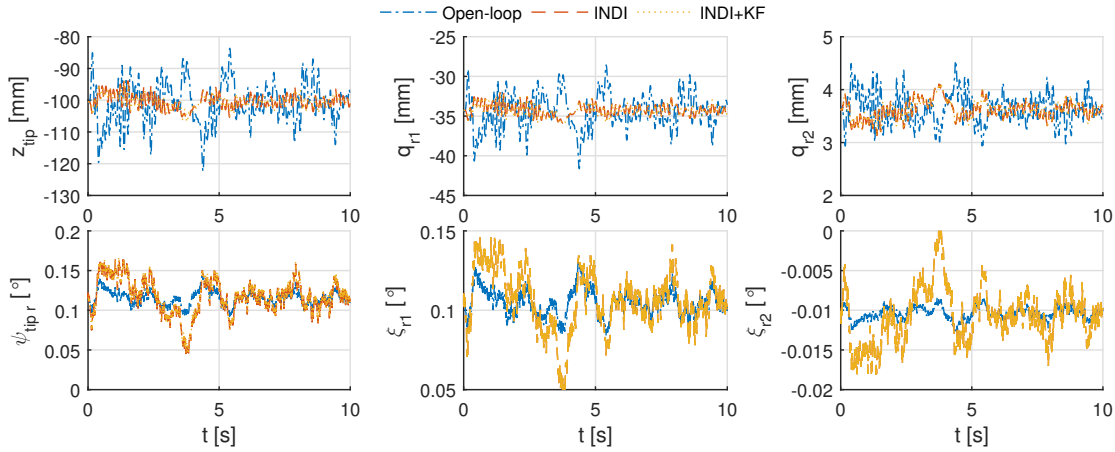

Fig. 13 Wing-tip bending, torsion and generalized displacements under turbulence excitation.

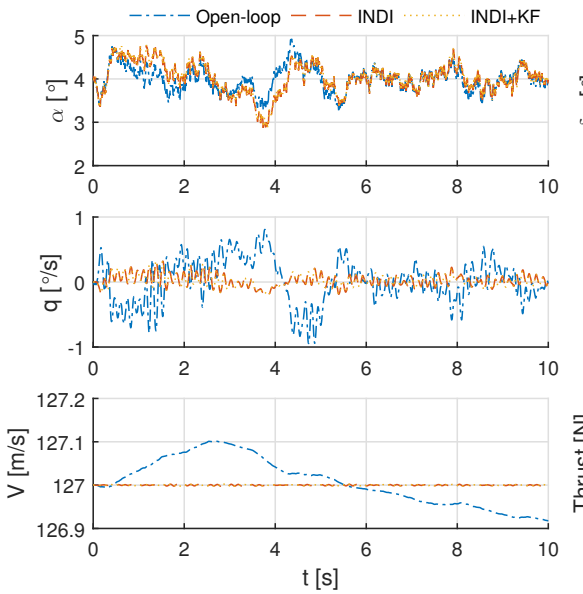

Fig. 14 Rigid-body state responses.

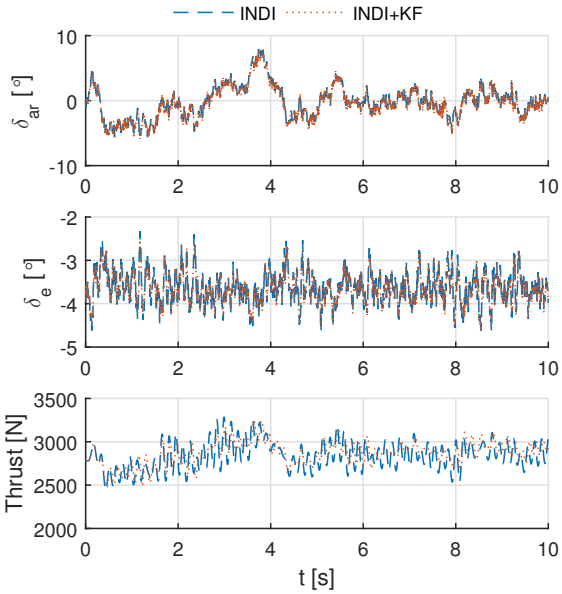

Fig. 15 Control inputs using INDI.

Table 3 The RMS, peaks of load and wing root bending moment increments under gust excitation.

	max $\lvert\Delta n_z\rvert$ [g]		$\hat{\sigma}_{\Delta n_z}$ [g]		max $\lvert\Delta M_r\rvert$ [kgm^2/s^2]		$\hat{\sigma}_{\Delta M_r}$ [kgm^2/s^2]	
Open-loop	0.4021		0.1186		4.02×10^4		1.14×10^4	
INDI	0.2604	35.2%	0.0722	39.1%	5.52×10^3	86.3%	1.52×10^3	86.8%

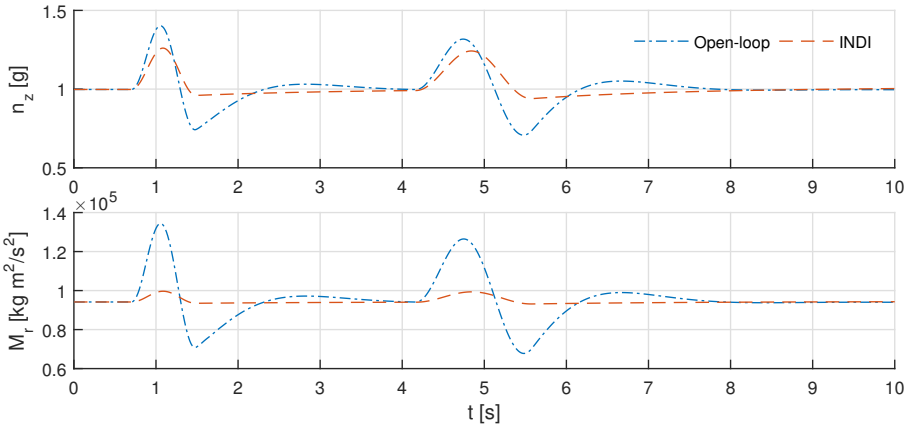

Fig. 16 Vertical load and wing root bending moment responses under gust excitation.

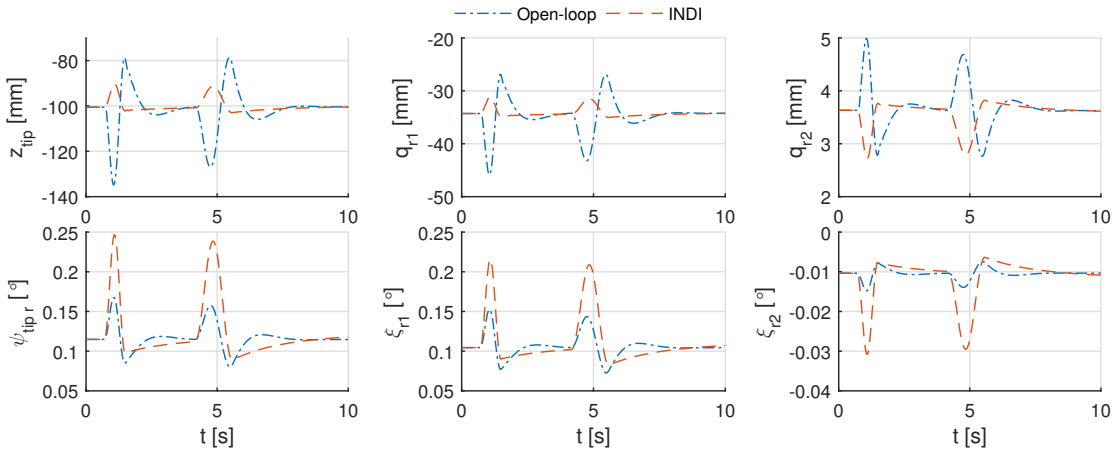

Fig. 17 Wing-tip bending, torsion and generalized displacements under gust excitation.

E. Robustness Analysis

Based on the derivations in Sec. III, it can be seen this INDI GLA controller is designed via a sensor-based approach, namely part of the dynamic model has been replaced by sensor measurements, which improves the robustness of this controller to aerodynamic model uncertainties. The linear proportional virtual control term $\boldsymbol{\nu}_p$ also contributes to enhancing the robustness [21]. According to Eq. (26), the only model information required by this controller is the value of A_e and B_e matrices, namely the aerodynamic forces related to elastic states and control inputs. Since $\boldsymbol{x}$ is continuously differentiable, $\lim_{\Delta t \to 0} \|\Delta \boldsymbol{x}\| = 0$. As a result, recall Eq. (20), the influences of model uncertainties in A_e matrix can be diminished by increasing the sampling frequency. The robustness of this controller will be tested numerically in this section.

The current aerodynamic model of the flexible aircraft is based on strip theory. The aircraft model contains k components, namely the fuselage (fu), engine pylon (p), wing (w), horizontal tail (ht), vertical tail (vt), elevator (ele), ailerons (ail), and rudder (ru). Each aircraft component is divided into n_k strips and the corresponding local lift coefficients are given at one preselected trim point [2]. In reality, the aerodynamics of flexible aircraft are uncertain and time varying. Therefore, the model is augmented by lift coefficient uncertainties $\Delta C_{L_\alpha k}$ for robustness analyses. First, different components are perturbed separately, and the uncertainties are set to be proportional to the nominal lift coefficients $C_{L_\alpha k_*}$ as expressed by

$$\Delta C_{L_\alpha k} \triangleq \rho_k C_{L_\alpha k_*}, \quad \rho_k \in [-1, 1], \quad k = fu, p, w, ht, vt, ele, ail, ru. \tag{36}$$

Since this paper deals with symmetric disturbance rejection, the uncertainties are added into the wing (w),

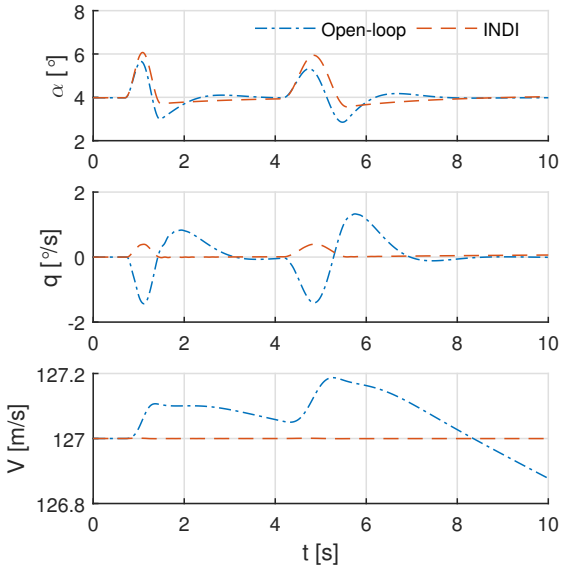

Fig. 18 Rigid-body state responses to gust.

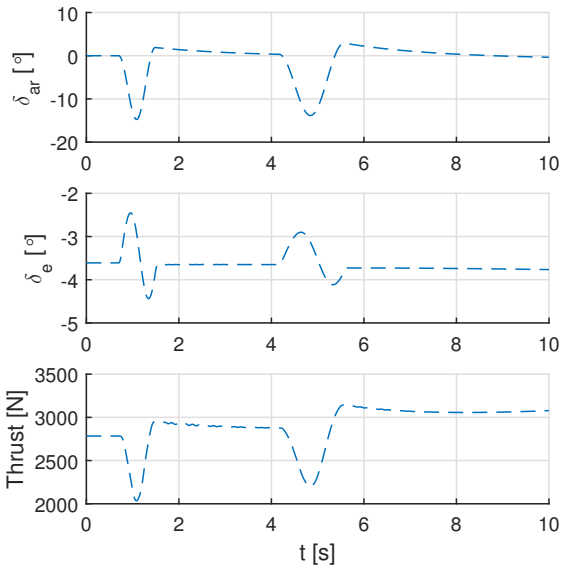

Fig. 19 Control inputs in a gust field.

horizontal tail (ht), elevator (ele) and ailerons (ail). Fig. 20 shows the GLA effectiveness in the presence of elevator and aileron aerodynamic model uncertainties. If the actual control surface lift coefficients are larger than modeled, the control surface may overact and potentially lead to oscillations. On the contrary, loss of control effectiveness (e.g. caused by control surface damages) would result in control surface saturations or even lost of control. As can been seen from Fig. 20, this controller is able to cope with a wide range of control surface uncertainties, namely $\rho_{ele} \in [-0.98, 1]$ and $\rho_{ail} \in [-0.81, 1]$. It can re-trim the aircraft and alleviate the gust load effectively unless more than 80% of control effectiveness has been lost.

As shown in Fig. 21, this controller is able to re-trim the aircraft and alleviate the gust load when $\rho_{hv} \in [-1, 1]$. The pitching moment variations caused by horizontal tail model uncertainties can be compensated by elevator deflections and thrust control. The range of wing model uncertainties that can be sustained by this controller is $\rho_w \in [-0.28, 0.20]$, which is narrower as compared to other ranges since wing lift has such dramatic influences on the aircraft dynamics.

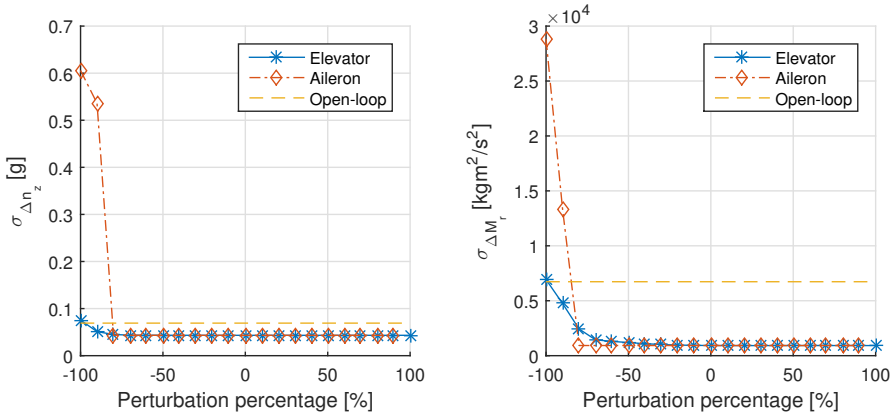

Fig. 20 GLA effectiveness in the presence of control surfaces aerodynamic uncertainties.

After perturbing different components separately, a Monte-Carlo simulation containing 1000 uncertain aerodynamic models is conducted to test the robustness of this controller to random combinations of

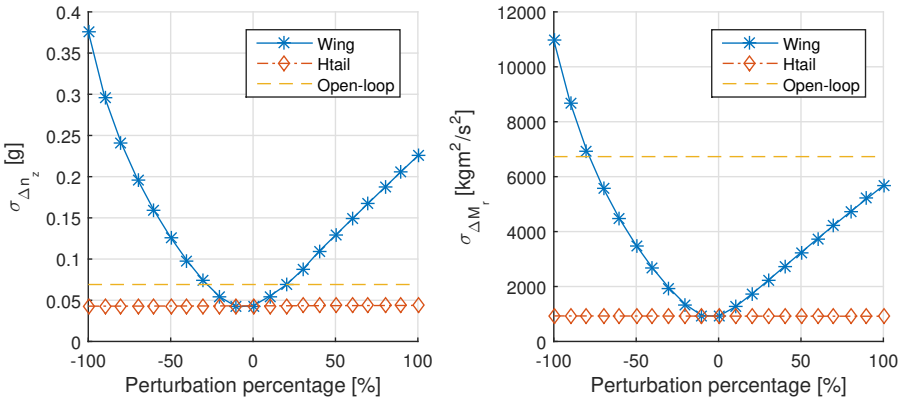

Fig. 21 GLA effectiveness in the presence of wing and tail aerodynamic uncertainties.

aerodynamic model uncertainties, modeled by

$$\Delta C_{L_\alpha k} \triangleq \{\Delta C_{L_\alpha k} \in \mathbb{R} | \Delta C_{L_\alpha k} = N(0, \sigma_k^2)\}, \quad \sigma_k = \rho_k C_{L_\alpha k_*}, \quad k = fu, p, w, ht, vt, ele, ail, ru. \tag{37}$$

For each component k, the mean value of uncertainty is zero and the standard deviation σ_k is chosen as ρ_k times the nominal lift coefficient value of this component. The perturbation range is chosen as $\rho_{ele} = \rho_{ail} = \rho_{hv} = 0.3$, $\rho_w = 0.1, \rho_{fu} = \rho_p = \rho_{vt} = \rho_{ru} = 0$. in this simulation.

As shown in Fig. 22, among the 1000 samples, the median value of the vertical load under INDI control is 0.0452 g, which has been alleviated by 34.6% as compared to the open-loop responses. The interquartile range (IQR) of n_z is only 0.01 g. Besides, all the tested samples present lower wing root bending moment as compared to the open-loop responses. The few larger RMS of load variations are caused by dramatic wing lift coefficient perturbations and long-term actuator saturations. This Monte-Carlo simulation further indicates the robust performance of the proposed controller to aerodynamic model uncertainties.

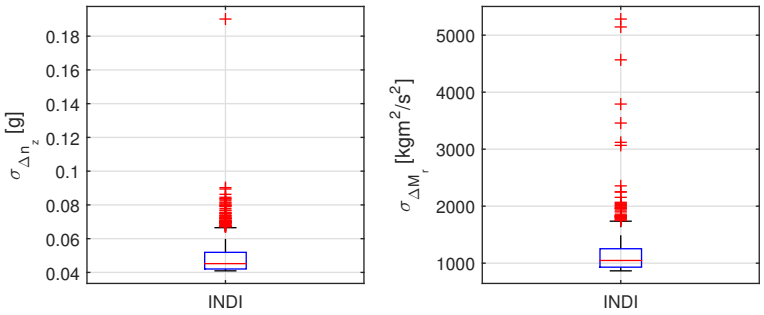

Fig. 22 Box plot of a Monte-Carlo simulation of the closed-loop system subjects to model uncertainties.

V. Conclusions

In this paper, an Incremental Nonlinear Dynamic Inversion (INDI) gust load alleviation (GLA) control law is designed for a flexible aircraft. A flexible aircraft model that encompasses both inertia and aerodynamic coupling effects between rigid-body dynamics and elastic vibration dynamics is presented. This flexible aircraft model is compare with a quasi-rigid aircraft model from the perspective of the trim and eigenvalue solutions. The coupling effects lead to different trim solutions for these two models and also distinguish the rigid-body modes of the flexible aircraft from the quasi-rigid aircraft modes.

The time scale separation principle for the flexible aircraft is redefined and verified numerically. Based on this principle, an incremental dynamic equation is derived for the original nonlinear system. The INDI GLA control law aims at load alleviation is then designed for the flexible aircraft. Besides, using the Kalman filter, the elastic deformations and deformation velocities are observed from accelerometer measurements. The fifth order Padé approximation is adopted to model the pure time delay in the state estimation.

Furthermore, time domain simulations of a flexible aircraft flying through various 2D spatial turbulence and gust fields verify the proposed INDI GLA controller can effectively suppress the rigid-body modes, alleviate the vertical load, reduce the wing root bending moment, and suppress the wing bending modes. Since this flexible aircraft configuration only has a pair of control surfaces on the wing, trade-offs need to be made between different control objectives. The performance of the present controller can be further enhanced if more control surfaces are available on the wing.

In addition, various perturbation tests and a Monte-Carlo simulation demonstrate the robustness of the proposed controller to aerodynamic model uncertainties. A wide range of control surface model mismatches can be tolerated by the controller without using any additional fault-tolerant control technique. This INDI GLA controller is also promising for maneuver load alleviation problems, even in the presence of loss of control effectiveness.

References

[1] Waszak, M. R., and Schmidt, D. K., "Flight Dynamics of Aeroelastic Vehicles," *Journal of Aircraft*, Vol. 25, No. 6, 1988, pp. 563–571. doi:10.2514/3.45623, URL http://arc.aiaa.org/doi/abs/10.2514/3.45623.

[2] Meirovitch, L., and Tuzcu, I., "Integrated Approach to the Dynamics and Control of Maneuvering Flexible Aircraft," Tech. rep., Virginia Polytechnic Institute and State University, 2003.

[3] Patil, M. J., Hodges, D. H., and S. Cesnik, C. E., "Nonlinear Aeroelasticity and Flight Dynamics of High-Altitude Long-Endurance Aircraft," *Journal of Aircraft*, Vol. 38, No. 1, 2001, pp. 88–94. doi:10.2514/2.2738, URL http://arc.aiaa.org/doi/10.2514/2.2738.

[4] Shearer, C. M., and Cesnik, C. E., "Nonlinear Flight Dynamics of Very Flexible Aircraft," *Journal of Aircraft*, Vol. 44, No. 5, 2007, pp. 1528–1545. doi:10.2514/1.27606, URL http://arc.aiaa.org/doi/10.2514/1.27606.

[5] Dillsaver, M., Cesnik, C., and Kolmanovsky, I., "Gust Load Alleviation Control for Very Flexible Aircraft," *AIAA Atmospheric Flight Mechanics Conference*, American Institute of Aeronautics and Astronautics, Portland, Oregon, 2011, pp. 1–18. doi:10.2514/6.2011-6368, URL http://arc.aiaa.org/doi/10.2514/6.2011-6368.

[6] Liebst, B. S., Garrard, W. L., and Farm, J. A., "Design of a multivariable flutter suppression/gust load alleviation system," *Journal of Guidance, Control, and Dynamics*, Vol. 11, No. 3, 1988, pp. 220–229. doi:10.2514/3.20297, URL http://arc.aiaa.org/doi/10.2514/3.20297.

[7] Nguyen, N. T., Swei, S., and Ting, E., "Adaptive Linear Quadratic Gaussian Optimal Control Modification for Flutter Suppression of Adaptive Wing," *AIAA Infotech @ Aerospace*, American Institute of Aeronautics and Astronautics, Kissimmee, Florida, 2015, pp. 1–23. doi:10.2514/6.2015-0118, URL http://arc.aiaa.org/doi/10.2514/6.2015-0118.

[8] Haghighat, S., T. Liu, H. H., and R. A. Martins, J. R., "Model-Predictive Gust Load Alleviation Controller for a Highly Flexible Aircraft," *Journal of Guidance, Control, and Dynamics*, Vol. 35, No. 6, 2012, pp. 1751–1766. doi:10.2514/1.57013, URL http://arc.aiaa.org/doi/abs/10.2514/1.57013.

[9] Fan, W., Liu, H. H., and Kwong, R., "Gust Load Alleviation Control for a Flexible Aircraft with Loss of Control Effectiveness," *AIAA Guidance, Navigation, and Control Conference*, American Institute of Aeronautics and Astronautics, Grapevine, Texas, 2017, pp. 1–16. doi:10.2514/6.2017-1721, URL http://arc.aiaa.org/doi/10.2514/6.2017-1721.

[10] Zeng, J., Moulin, B., de Callafon, R., and Brenner, M. J., "Adaptive Feedforward Control for Gust Load Alleviation," *Journal of Guidance, Control, and Dynamics*, Vol. 33, No. 3, 2010, pp. 862–872. doi:10.2514/1.46091, URL http://arc.aiaa.org/doi/abs/10.2514/1.46091.

[11] Sieberling, S., Chu, Q. P., and Mulder, J. A., "Robust Flight Control Using Incremental Nonlinear Dynamic Inversion and Angular Acceleration Prediction," *Journal of Guidance, Control, and Dynamics*, Vol. 33, No. 6, 2010, pp. 1732–1742. doi:10.2514/1.49978, URL http://arc.aiaa.org/doi/abs/10.2514/1.49978.

[12] Simplício, P., Pavel, M., van Kampen, E., and Chu, Q., "An acceleration measurements-based approach for helicopter nonlinear flight control using Incremental Nonlinear Dynamic Inversion," *Control Engineering Practice*, Vol. 21, No. 8, 2013, pp. 1065–1077. doi:10.1016/j.conengprac.2013.03.009, URL http://dx.doi.org/10.1016/j.conengprac.2013.03.009.

[13] Wang, X., Van Kampen, E.-J., and Chu, Q. P., "Gust Load Alleviation and Ride Quality Improvement with Incremental Nonlinear Dynamic Inversion," *AIAA Atmospheric Flight Mechanics Conference*, American Institute of Aeronautics and Astronautics, Grapevine, Texas, 2017, pp. 1–21. doi:10.2514/6.2017-1400, URL http://arc.aiaa.org/doi/10.2514/6.2017-1400.

[14] Lu, P., van Kampen, E.-J., de Visser, C., and Chu, Q., "Aircraft fault-tolerant trajectory control using Incremental Nonlinear Dynamic Inversion," *Control Engineering Practice*, Vol. 57, 2016, pp. 126–141. doi:10.1016/j.conengprac.2016.09.010, URL http://dx.doi.org/10.1016/j.conengprac.2016.09.010.

[15] Smeur, E. J. J., Chu, Q. P., and de Croon, G. C. H. E., "Adaptive Incremental Nonlinear Dynamic Inversion for Attitude Control of Micro Air Vehicles," *Journal of Guidance, Control, and Dynamics*, Vol. 39, No. 3, 2016, pp. 450–461. doi:10.2514/1.G001490, URL http://arc.aiaa.org/doi/10.2514/1.G001490.

[16] *U.S. Military Specification MIL-F-8785C*, 1980.

[17] Etkin, B., *Dynamics of Atmospheric Flight*, Dover Publications, Toronto, 2005. doi:10.1007/s13398-014-0173-7.2.

[18] Nam, C., Kim, Y., and Layton, J., "Active Aeroelastic Wing Design for Gust Load Alleviation and Flutter Suppression," *38th Structures, Structural Dynamics, and Materials Conference*, American Institute of Aeronautics and Astronautics, Kissimmee, Florida, 1997, pp. 729–737. doi:10.2514/6.1997-1265, URL http://arc.aiaa.org/doi/10.2514/6.1997-1265.

[19] Bacon, B., and Ostroff, A., "Reconfigurable flight control using nonlinear dynamic inversion with a special accelerometer implementation," *AIAA Guidance, Navigation, and Control Conference and Exhibit*, American Institute of Aeronautics and Astronautics, Denver, CO, 2000, pp. 1–15. doi:10.2514/6.2000-4565, URL http://arc.aiaa.org/doi/10.2514/6.2000-4565.

[20] Nguyen, N. T., Ting, E., Nguyen, D. Y., and Trinh, K. V., "Flight Dynamic Modeling and Stability Analysis of Flexible Wing Generic Transport Aircraft," *55th AIAA/ASME/ASCE/AHS/ASC Structures, Structural Dynamics, and Materials Conference*, American Institute of Aeronautics and Astronautics, National Harbor, Maryland, 2014. doi:10.2514/6.2014-1040, URL http://arc.aiaa.org/doi/10.2514/6.2014-1040.

[21] Khalil, H. K., *Nonlinear Systems*, Prentice-Hall, New Jersey, 2002.

This article has been cited by:

1. Paul Acquatella, Erik-Jan Van Kampen, Qi P. Chu. A Sampled-Data Form of Incremental Nonlinear Dynamic Inversion for Spacecraft Attitude Control . [Abstract] [PDF] [PDF Plus]
2. Jinglong Liu, Zhonghua Wu, Xiaowen Xing, Qizhi He. 2020. Barrier Lyapunov function and disturbance observer based omnidirectional robust gust response stabilization for multi-control-effectors aircraft. *Aircraft Engineering and Aerospace Technology* **92**:6, 777-799. [Crossref]
3. X. Wang, E. Van Kampen, Q. P. Chu, Roeland De Breuker. 2019. Flexible Aircraft Gust Load Alleviation with Incremental Nonlinear Dynamic Inversion. *Journal of Guidance, Control, and Dynamics* **42**:7, 1519-1536. [Abstract] [Full Text] [PDF] [PDF Plus]
4. Stefan A. Raab, Jiannan Zhang, Pranav Bhardwaj, Florian Holzapfel. Consideration of Control Effector Dynamics and Saturations in an Extended INDI Approach . [Citation] [PDF] [PDF Plus]
5. Xuerui Wang, Erik-Jan van Kampen, Qiping Chu, Peng Lu. 2019. Stability Analysis for Incremental Nonlinear Dynamic Inversion Control. *Journal of Guidance, Control, and Dynamics* **42**:5, 1116-1129. [Abstract] [Full Text] [PDF] [PDF Plus]
6. Stefan A. Raab, Jiannan Zhang, Pranav Bhardwaj, Florian Holzapfel. Proposal of a Unified Control Strategy for Vertical Take-off and Landing Transition Aircraft Configurations . [Citation] [PDF] [PDF Plus]